Design and Construction of an Apparatus for the Neutral Dissociation and Ionization of Molecules in an Intense Laser Field

A Thesis Presented

by

Patrick Henning Nürnberger

to

The Graduate School

in Partial Fulfillment of the Requirements

for the Degree of

Master of Arts

in

Physics

State University of New York
at
Stony Brook

May 2003

State University of New York
at Stony Brook

The Graduate School

Patrick Henning Nürnberger

We, the thesis committee for the above candidate for the Master of Arts degree, hereby recommend acceptance of the thesis.

Professor Thomas C. Weinacht, Thesis Advisor
Department of Physics and Astronomy

Professor Luis A. Orozco
Department of Physics and Astronomy

Professor Alexandre Abanov
Department of Physics and Astronomy

This thesis is accepted by the Graduate School.

Graduate School

Abstract of the Thesis

Design and Construction of an Apparatus for the Neutral Dissociation and Ionization of Molecules in an Intense Laser Field

by

Patrick Henning Nürnberger

Master of Arts

in

Physics

State University of New York at Stony Brook

2003

We have designed and constructed an apparatus for studying neutral dissociation of molecules using shaped ultrashort laser pulses. The apparatus consists of a femtosecond laser oscillator, a chirped pulse amplifier, a shaped–pulse Mach-Zehnder interferometer, a device to measure the duration and structure of the light pulses (FROG), a molecular beam and a time–of–flight mass spectrometer. We have made preliminary measurements to show that the apparatus is suitable for pump–probe learning control of neutral dissociation.

To Anne and my family

Contents

List of Figures

List of Tables

Acknowledgements

In my first week at Stony Brook I visited Tom Weinacht's office, for whom it was the first week at Stony Brook as well. We talked about the research he was intending to do, when he said what erased my last hesitations: "The disadvantage to work in a new lab is that you have to build up things, but the advantage is...that you have to build up things."

I am very grateful that I was given the opportunity to take this challenge and to help building an experiment that combines latest ultrafast laser setups, vacuum techniques, mass spectrometry and coherent control mechanisms, as well as a lot of engineering and machining. I am really obliged to Tom for the cooperation and guidance during the project.

I am also very pleased to acknowledge the cooperation with and the assistance of David Cardoza. The countless days and nights we spent together in the lab were really fun and I enjoyed them very much, from simple day–to–day things like laser alignment over hours of software despair or data delight, to the entertaining anecdotes when we took bricks out of the wall or produced a fountain in the lab when we tested our plumbing skills.

Furthermore I want to thank Frank Dimler who solved all the problem sets of our classes with me and without whom I would have had a much harder

time at Stony Brook. During the second half of the project, Dominik Maxein joined the group and always was a helpful and humorous support. Also, the lab work was much more cheerful with the Orozco lab students Susan Metz, Joe Reiner, Matt Terraciano, Seth Aubin, and Eduardo Gomez next door. Thank you all for contributing to my work in some way.

I am thankful to the Department of Physics and Astronomy, the machine shop and the chemistry glass shop. I also acknowledge the Bayerische Julius–Maximilians–Universität Würzburg and their exchange program with Stony Brook. A scholarship from the State of Bavaria (“Stipendium nach dem Bayerischen Begabtenförderungsgesetz”) and the German Merit Foundation (“Studienstiftung des deutschen Volkes”) provided the financial framework and is highly appreciated, too.

I also want to acknowledge the Research Corporation for providing funding for this project.

I would also like to thank my parents for always encouraging me and giving me the opportunities that allowed me to reach this point.

Finally, I’d like to thank Anne for her neverending love and support.

Patrick Henning Nürnberger

Stony Brook, Long Island

May 2003

Chapter 1

Introduction

Ultrashort lasers provide us with an excellent tool for a large variety of applications. They can be used to monitor rapidly evolving processes in liquids, solids and in the gas phase, to scan sensitive surfaces, to achieve huge energy densities, to attain nonlinear optical effects, to control molecular dynamics and chemical reactions, and for many other applications not limited to physics.

There are many things that have driven the recent advances in coherent control. Two important contributions have been the greatest benefit to the community: the development of broadband lasers and the development of learning control. At the beginning of the 1990s the development of short pulse Titanium Sapphire lasers [17, 18] caused something of a revolution in the field of ultrafast lasers, for they produce stable modelocking, have enormous bandwidths and large energy storage capabilities. This powerful and excellent instrument opened a whole new field of physics and chemistry.

These lasers can be used to get access to new chemical reaction channels, *i. e.* to processes that could not be caused without laser assistance. Also at the beginning of the 1990s, the concept of learning control was developed. The electric field of the laser pulse is actively changed by a pulse shaper that allows to create almost any desired pulse, with the bandwidth of the pulse as only sharp limit. Thus, a pulse shape that is suitable for a certain reaction can be achieved. Rabitz *et al.* introduced the scheme of feedback–control, where the effects of the laser pulse shape are used to create the next generation of pulse shapes. Lasers have been successfully used to get access to new chemical reaction channels, *i. e.* to processes that could not be caused without laser assistance. For example, intense ultrashort laser pulses can create non–thermal distributions that can lead to breaking a strong bond in the presence of a weaker one.

Evidences that this approach can actually be used to optimize a certain process or reaction have been shown in the mid-90s [40], which proved that it is possible to control a chemical system with no knowledge *a priori* of the involved Hamiltonians. Learning control experiments have successfully demonstrated control over dissociative ionization, vibrational excitation, higher harmonic generation, and much more.

Parallel to this vast development of applications for ultrashort lasers, their efficiency and power has been more and more improved. Femtosecond laser pulses that are shorter than 10 fs have been created [23, 22], and a variety of excellent amplifier systems (optical parametric amplifier, chirped pulse amplifier,. . .) were designed to increase the realizable output powers. The intensity regime of magnitude 10^{15} Wcm^{-2} and higher can nowadays be accessed with most amplifier systems, allowing to make experiments just one order of magnitude below the atomic unit of intensity $3.51 \cdot 10^{16}$ Wcm^{-2}.

The aim of the project described in this thesis was to design and construct an apparatus that is suitable for learning control experiments with molecules in the gas phase. Therefore, a femtosecond laser system as well as a vacuum system had to be built. We designed and built a time–of–flight (TOF) spectrometer because it is a very useful accurate apparatus, as it gives the mass distribution of detected ions and information about initial kinetic energy for an ensemble of molecules. This direct information can be recorded and analyzed for each single laser pulse. It is particularly useful for looking at dissociation processes, although it only works for ions. As we want to investigate neutral dissociation, we built a pump–probe setup, where a shaped laser beam (pump) causes the neutral dissociation, while a succeeding intense pulse (probe) after a changeable time period ionizes the fragments, so that they can be detected by the time–of–flight spectrometer. Ever since the pioneering paper by Wiley and McLaren [33] time–of–flight ion (TOF) spectrometers have been an important tool in molecular spectroscopy.

We start this thesis with a very brief description of the basic and necessary theory about the optics involved in chapter 2. This includes modelocking, the nonlinear polarization, Kerr Lens mode locking and others. We then continue with installation of the femtosecond laser oscillator and the chirped pulse amplifier. Afterwards we introduce a “FROG” (Frequency Resolved Optical Gating), a device that allows us to measure the full electric field of ultrashort laser pulses.

Chapter 3 discusses the design of the vacuum chamber, preceded by a short introduction of the necessary formulas. The description of microchannel plates refers to the explanation of the construction of the detector region that follows. Finally, an overview of the whole setup is given in the last pages of that chapter.

When one has built something over several months one cannot but want to see it work. The first experimental results taken with the apparatus are shown in chapter 4, where TOF data was taken for air, methanol and benzene. The last chapter deals with the most interesting acetone data from pump probe measurements, *i. e.* with two incoming laser beams at controllable time differences. Several known properties could be verified, but also a few new features appeared that might be interesting for further experiments in the future.

Chapter 2

Optics

In order to understand how the laser system works that is used to generate the necessary intensities for the final experiment, a brief discussion of the basic mathematics of the optical phenomena involved will be presented in the following sections.

2.1 Modelocking

A laser is normally lasing in a few longitudinal modes, which are separated by $\Delta\nu = \frac{c}{2L}$, where L is the length of the cavity. How many modes actually contribute is determined by the loss in the cavity and the gain bandwidth (and other things like the actual pump power,broadening mechanisms, $\ldots$). If the phases of the independent modes inside the cavity are random, the modes form a diffuse beat, with a fluctuating amplitude behavior, as it can be seen in figure 2.1 in the left picture, where 12 longitudinal modes with random phases are shown. In order to achieve large intensities, it is desirable to lock the phase

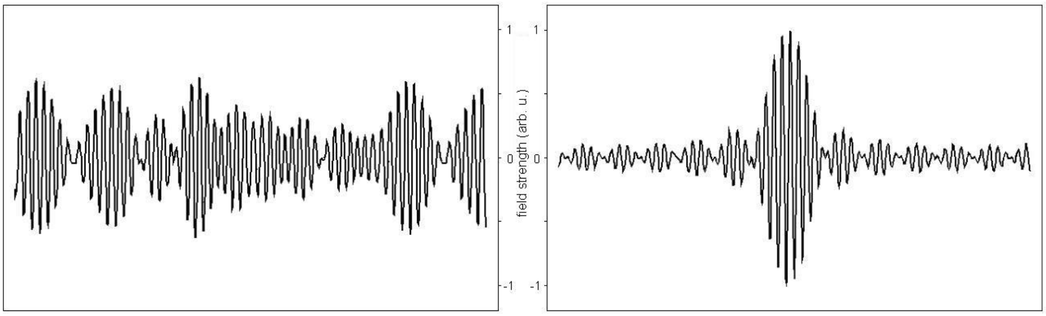

Figure 2.1: Sum of the electric field of 12 longitudinal laser modes with random and modelocked phases inside a cavity

of the modes, *i. e.* to give adjacent modes a well-defined phase difference. The right side of figure 2.1 shows the amplitude for 12 modes with a constant phase difference; they are "modelocked". The sum of the electric field of N adjacent modelocked modes takes the form:

$$\mathbf{E}(r=0,t) = \sum_{j=-N/2}^{N/2} \mathbf{E}_0 \sin([\omega_0 + j \cdot 2\pi\Delta\nu]t + \phi) =$$

$$\mathbf{E}_0 \sin(\omega_0 t + \phi) \frac{\sin(N\pi\Delta\nu t)}{\sin(\pi\Delta\nu t)} \tag{2.1}$$

where $\Delta\nu$ is the mode spacing, ϕ is the locked phase, and for simplicity r is set to zero and all amplitudes have the same magnitude and polarization. The form of the field is therefore given by a function $\sin(Nx)/\sin(x)$ for large N and the more modes contribute, the more the electric field is peaked, as it can be seen it figure 2.1. The pulse peak has a width of $\frac{2L}{cN}$ and repeats after $t = \frac{1}{\Delta\nu} = \frac{2L}{c}$, which represents the round trip time in the cavity. In the laser oscillator (KM Labs Model TS) in our laboratory about half a million longitudinal modes are lasing and modelocked. Thus, the pulses durations lie in the femtosecond regime.

To achieve modelocked operation of a laser, one has to find a way to couple the phases. There are mainly two ways to get a laser to modelock: active and passive modelocking. If an actual physical device is used to do this, one speaks of active modelocking. As there is nothing like a shutter that can open just for the short pulse duration, one has to think of another possibility to generate pulses. For example lasers have been built where an intracavity loss modulator at the frequency $\Delta\nu$ allows the formation of pulses, although not in the ultrashort regime [12]. Passive modelocking does not involve a mechanism driven from outside the laser resonator. If a loss–mechanism that depends on the intensity is introduced into the cavity, small fluctuations in the continous–wave laser beam could be amplified, while weaker parts of the beam would become weaker and weaker, until only one intense pulse is left. This can be achieved via *e. g.* a saturable absorber.

A special way of passive modelocking is “self–modelocking”, where the active medium itself acts as a material with an intensity–dependent gain–loss profile. The femtosecond laser oscillator in our experiment is a Ti:Sapphire crystal that is appropriate for self–modelocking and the Kerr lens effect (see later in section 2.3.2).

2.2 Group Velocity and Chirp of Pulses

The optical pulses used for this thesis have a broad spectral bandwidth. It is useful to introduce the spectral width of the pulse as $\Delta f = FWHM$ (full width at half max) of the intensity spectrum, and also its pulse duration $\Delta t = FWHM$ of the intensity over time. From Fourier analysis we know that t and ν are conjugate variables, therefore a pulse is limited by the relation [3]

$$\Delta f \cdot \Delta t \geq k \tag{2.2}$$

where the constant k is of the order of unity[1]. A pulse is called "transform–limited" if its duration is minimal for the given bandwidth, *i. e.* if the equal–sign in (2.2) applies.

The bandwidth of the pulse leads to interesting effects when the pulse propagates through a dispersive medium. If different frequencies of the beam see different indices of refraction, not every frequency gets the same phaseshift, and the group velocity will change if the phase velocity dispersion is of higher order than one. In a region of normal dispersion for example it will take longer for a blue ray to traverse the medium than it takes for a red one. The transform–limited pulse, which is nothing else but a wavepacket, gets spread out by this effect. The pulse is moving through the medium with the group velocity v_G, which is defined as:

$$v_G = \frac{d\omega}{dk}|_{k_0} \tag{2.3}$$

---

[1] The value of k depends on the actual shape of the pulse. It can be smaller than one, see example in [11], where it is 0.315

with the central wave vector k_0. This equation can be rewritten using the relation:

$$\omega = \frac{ck}{n(k)} \tag{2.4}$$

with the speed of light c in vacuum, the absolute value of the vacuum wave vector k and the wavelength–dependent index of refraction $n(k)$, so that we come to the result:

$$v_G = \frac{c}{n(k_0)} \left(1 - \frac{k_0}{n(k_0)} \frac{dn(k)}{dk} |_{k_0} \right) \tag{2.5}$$

Therefore, if the index of refraction is dependent on the wavelength, the group velocity is changing. A measure to describe this change is the "group velocity dispersion" or GVD, defined as:

$$GVD = \frac{d^2 k}{d\omega^2} \tag{2.6}$$

In substances with normal dispersion, the GVD is positive and after going through the material low frequency components can be found earlier than high frequency ones in a formerly transform–limited pulse , *i. e.* the pulse acquired a positive "chirp" (see Figure 2.2, where the chirp is positive if the direction of propagation is towards the left). If

$$\frac{d^i \omega}{dk^i} \tag{2.7}$$

is equal to zero for all $i > 2$, the chirp is linear, if higher terms exist, the shape of the pulse is more complicated and it is *e. g.* also possible that blue is followed by red and then by blue again.

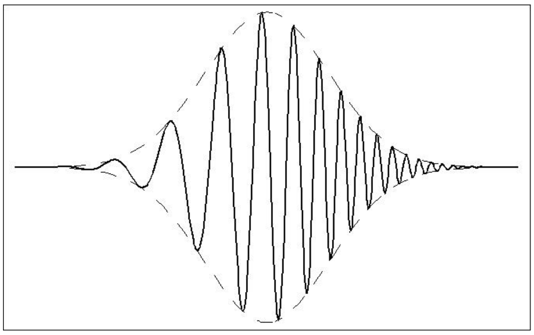

Figure 2.2: Electric field of a linearly chirped pulse

To provide a convenient description of the phase of $\mathbf{E}(t)$ after a pulse has passed through a dispersive material, one can make a Taylor expansion of the phase around the middle of the temporal intensity profile [28]:

$$\varphi(t) = \sum_{i=1}^{\infty} \frac{1}{i!} A_i t^i \tag{2.8}$$

where the coefficients A_i are given by:

$$A_i = \frac{d^i \varphi(t)}{dt^i}|_0 \tag{2.9}$$

A closer look tells us that A_0 is just a constant phase term and A_1 is the angular frequency at the middle of the pulse. The case where $A_2 > 0$ corresponds to the earlier positive chirp, and if $A_i \neq 0$ for $i > 2$ higher order dispersion can be observed.

When designing a modelocked titanium sapphire oscillator it is desirable to compensate for the dispersion that is produced inside the crystal gain medium, so a setup is used which introduces a negative GVD (or a negative

A_2) to the pulse. Devices like prism pairs or gratings can only compensate for GVD, *i. e.* second–order dispersion. The invention of chirped mirrors, a mirror where the penetration depth and thus the plane of reflection depends on the wavelength, made it possible to compensate for higher orders of dispersion [22].

2.3 The Nonlinear Polarization

In many applications of physics, one can treat the electrons in an atomic medium as classical oscillators. When an electric field **E** penetrates such a medium, there is a response due to these oscillators inside the material. Assuming a totally isotropic medium and a linear response the following relations for the electric field **E**, the polarization **P** and the displacement **D** can be obtained [4]:

$$\mathbf{D} = \varepsilon\varepsilon_0\mathbf{E} = \varepsilon_0\mathbf{E} + \mathbf{P} \tag{2.10}$$

$$\mathbf{P} = \varepsilon_0\chi\mathbf{E} \tag{2.11}$$

where the quantity $\chi = \varepsilon - 1$ is the electric susceptibility.

This linear approximation is only valid in the limit of low electric field. Otherwise higher–order terms have to be taken into account. So in an experiment involving a laser with intense ultrashort pulses the linear response is not valid. However, one may expand the polarization in a series [11]:

$$\mathbf{P} = \sum_{n=1}^{\infty} \chi^{(n)}\mathbf{E}^n \tag{2.12}$$

The coefficients $\chi^{(n)}$ are the higher–order susceptibilities and are tensors of rank $n+1$ ([7]-[10]). However, the tensor indices will be suppressed, because they are not necessary for a basic understanding of the effects for which we will need formula (2.12). As long as the damage threshold of the material (on the order of the electric field of the atoms) is not reached, equation (2.12) is valid and can be rewritten for simplicity:

$$\mathbf{P} = \varepsilon_0 \chi^{(1)} \mathbf{E} + \varepsilon_0 \chi^{(2)} \mathbf{E}^2 + \varepsilon_0 \chi^{(3)} \mathbf{E}^3 + O(\mathbf{E}^4) \tag{2.13}$$

Obviously the polarization can be split into the linear polarization (first term) and the nonlinear polarization (higher terms), which is responsible for nonlinear effects. The second–order susceptibility $\chi^{(2)}$ for example describes second harmonic generation and the Pockels effect, $\chi^{(3)}$ gives rise to two photon absorption, third harmonic generation, the induced Raman effect, an intensity–dependent index of refraction, the Optical Kerr effect, self–focussing and self–phase modulation [14]. Some of these effects are important for the Master thesis project and will therefore be discussed in the following sections.

2.3.1 Second–Harmonic Generation

We make use of second–harmonic generation to measure the actual duration of the femtosecond pulses (see section 2.6). In high intensity fields the nonlinear terms in (2.13) become important. In the simple picture [2] of an incoming field of the form $\mathbf{E} = \mathbf{E}_0 \sin(\omega t)$ the formula (2.13) can be rewritten as:

$$\mathbf{P} = \varepsilon_0 \chi^{(1)} \mathbf{E}_0 \sin(\omega t) + \varepsilon_0 \chi^{(2)} \mathbf{E}_0^2 \sin^2(\omega t) + \varepsilon_0 \chi^{(3)} \mathbf{E}_0^3 \sin^3(\omega t) + O(\mathbf{E}^4) \tag{2.14}$$

which can be further simplified to

$$\begin{aligned}\mathbf{P} = \varepsilon_0\chi^{(1)}\mathbf{E}_0\sin(\omega t) + \frac{\varepsilon_0\chi^{(2)}}{2}\mathbf{E}_0^2[1-\cos(2\omega t)] \\ +\frac{\varepsilon_0\chi^{(3)}}{4}\mathbf{E}_0^3[3\sin(\omega t)-\sin(3\omega t)] + O(\mathbf{E}^4)\end{aligned} \tag{2.15}$$

The first term is a polarization that is varying with the same frequency as the incident electric field. The nonlinear term proportional to $\mathbf{E}_0^2$ consists of a constant polarization (responsible for optical rectification), and of a contribution to the polarization that is oscillating twice as fast as the incoming light wave. Therefore, it can radiate an electromagnetic wave with frequency 2ω, the second–harmonic. Analogously the term proportional to $\mathbf{E}_0^3\sin(3\omega t)$ can lead to third–harmonic generation. The question might arise: Why does one not observe second–harmonic generation at each lens or window that an intense beam is passing through? The reason is that in an isotropic medium like gases or liquids or in crystals with an inversion center, a reversal of the axes leads to a contradiction in (2.13) unless $\chi^{(2)}$ is equal to zero [5]:

$$-\mathbf{P}^{(2)} = \varepsilon_0\chi^{(2)}(-\mathbf{E})^2 = +\mathbf{P}^{(2)} \tag{2.16}$$

Therefore, only materials that are non-centrosymmetric exhibit second–harmonic generation. Furthermore, a frequency–dependent index of refraction makes it impossible to observe coherent second–harmonic light. If at one point of the crystal light at 2ω is produced, it will not be in phase with the light generated behind that point, because the initial wave that generates it sees a different index of refraction. In order to overcome this problem one has to use a birefringent crystal and cut it in such a way that phase matching is achieved, *i. e.* that light with both ω and 2ω see the same dispersion. Birefringent materials like potassium–dihydrogen phosphate (KDP), ammonium–dihydrogen phosphate (ADP), β–barium borate (BBO) or barium titanate ($BaTiO_3$) can be cut in such a way that this condition is achieved for a certain direction of incidence [6].

2.3.2 Optical Kerr Effect

In a medium with $\chi^{(2)} = 0$ there is no second–harmonic generation and if the phase–matching condition is not met also no significant third–harmonic can be observed. Thus, formula (2.15) takes the form:

$$\mathbf{P} = \varepsilon_0 \chi^{(1)} \mathbf{E}_0 \sin(\omega t) + \frac{3\varepsilon_0 \chi^{(3)}}{4} \mathbf{E}_0^3 \sin(\omega t) + O(\mathbf{E}^4) \tag{2.17}$$

which can be rewritten as:

$$\mathbf{P} = \varepsilon_0 \left(\chi^{(1)} + \frac{3\chi^{(3)}}{4} \mathbf{E}_0^2 \right) \mathbf{E}_0 \sin(\omega t) + O(\mathbf{E}^4) \tag{2.18}$$

The displacement $\mathbf{D}$ in equation (2.10) yields an expression for ε:

$$\varepsilon = \varepsilon_0 \left(1 + \chi^{(1)} + \frac{3\chi^{(3)}}{4} \mathbf{E}_0^2 \right) = \varepsilon_l + \varepsilon_{nl} \tag{2.19}$$

where $\varepsilon_l = 1 + \chi^{(1)}$ is just the linear expression for the dielectric permittivity, while $\varepsilon_{nl} = \frac{3}{4}\chi^{(3)}\mathbf{E}_0^2$ is the nonlinear contribution. The index of refraction, defined as $n = \sqrt{\varepsilon}$, therefore takes the form

$$\begin{aligned} n \;=\; \sqrt{\varepsilon} \;=\; \sqrt{\varepsilon_l + \varepsilon_{nl}} \approx \sqrt{\varepsilon_l} \cdot \left(1 + \frac{\varepsilon_{nl}}{2\varepsilon_l} \right) &= \\ n_l + \frac{3\chi^{(3)}}{8n_l} \mathbf{E}_0^2 \;=:\; n_0 + n_2 \cdot I(t) & \end{aligned} \tag{2.20}$$

So the index of refraction comprises the “ordinary” part plus a contribution that is proportional to the intensity of the light wave [6, 11]. It should also be mentioned that the contribution n_2 is always larger than zero [10]. A medium that shows this behavior is called a “Kerr medium”.

2.3.3 Self–Focussing and Self–Phase–Modulation

In the experiment we will deal with Gaussian femtosecond pulses, i.e. the beam has a Gaussian shape in the transverse spatial as well as in the temporal domain. The spatial distribution in a Kerr medium leads to the effect of self–focussing, while in the time domain it causes the self–phase modulation. A Gaussian beam with a large radius of curvature can be regarded as an approximately plane wave when it encounters the Kerr medium. Due to the intensity distribution over the beam cross section, the center sees a larger index of refraction than the wings. The result is that the beam phase fronts become increasingly concave (see figure 2.3, [16]), just as if they went through a lens. Therefore also the name “Kerr lens effect”. This constitutes soft aperture modelocking, where the self–focussing improves the overlap between the cavity mode and the pump beam, increasing the gain for modelocked operation. In hard aperture modelocking, a physical aperture is placed in the cavity, which increases losses for the continuous–wave (cw) mode.

The optical Kerr effect also has an impact on the phase of the wave. If the total phase behaves like $\mathbf{kr}$, where $\mathbf{k}$ is the wave vector, the phase changes

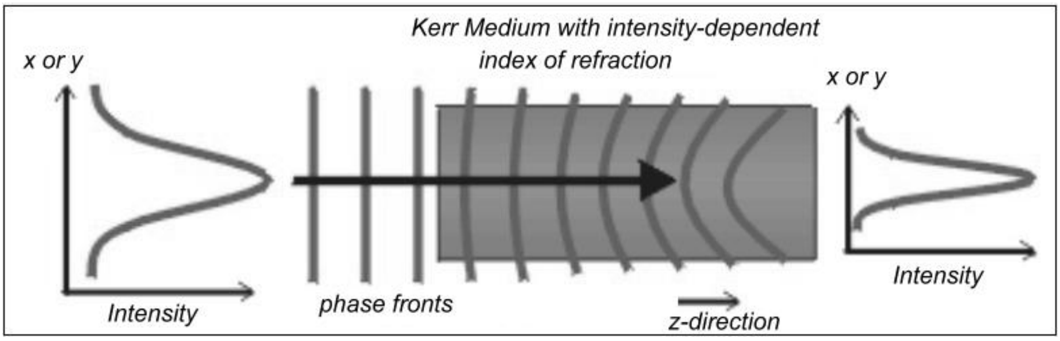

Figure 2.3: Self–focussing of an intense laser beam in a Kerr medium

when entering the Kerr medium:

$$\mathbf{k}\mathbf{r} = \frac{\omega_0}{c}(n_0 + n_2 I(t))\hat{\mathbf{k}}_0\mathbf{r} \tag{2.21}$$

which has a time–dependent phase correction

$$\phi(t, \mathbf{r}) = -\mathbf{k}_0\mathbf{r}n_2 I(t) \tag{2.22}$$

Just like in FM radio this phase modulation leads to the formation of several sidebands, so that the frequency spectrum of the pulse gets broadened. Furthermore, the phase between adjacent longitudinal modes is fixed, what leads to a coupling between the modes and makes them lock together to a pulse. Thus, the optical Kerr effect gives rise to the "self–phase modulation" and can act like a passive modelocking device (see section 2.1) [1, 14]. Self–phase–modulation gives rise to broader bandwidths than any other effect; it can be enhanced using optical fibers in which self–phase–modulation occurs [13].

2.4 The Ti:Sapphire oscillator

The experiment needs very short laser pulses, so in order to generate these a Ti:Sapphire ($Ti : Al_2O_3$) oscillator had to be set up. Ti:Sapphire has a gain bandwidth from 700 to 1100 nm, a very good thermal conductivity and is able to store energy densities up to 1 J/cm^2 [24]. Furthermore, it is a Kerr medium and therefore can be used as a self–modelocking laser medium. Very short laser pulses (< 10 fs) have been generated using Ti:Sapphire oscillators [21, 22, 23], which only consist of a few cycles of the electric field.

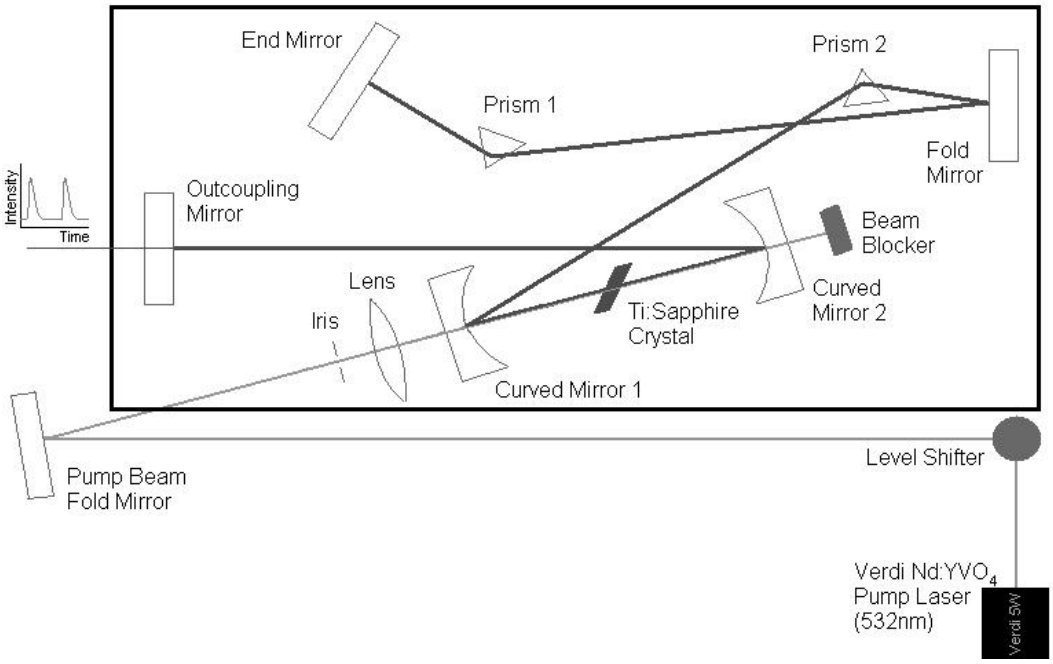

Figure 2.4: Ti:Sapphire oscillator setup

The laser we bought came in a kit from KM Labs (KM Labs Model TS). The setup is mainly the same as in the pioneering paper [17] or in [24] and can be seen in figure 2.4. The Brewster–angled crystal is in the center of the cavity and cut in such a way that the polarization of both the pump laser and the amplified pulse lie along the axis where the gain is largest. The population inversion inside the crystal is achieved using a pump beam from a $Nd:YVO_4$ cw laser (Verdi) at 532 nm which we usually operate at 4.30 W. It is focussed right into the crystal and enters the cavity through 'curved mirror 1' (see figure 2.4), which is highly reflective for the 800 nm range but transparent for the green pump beam. Once many modes start to lase, it is difficult for them to stay in phase because of dispersion. As the laser beam has to travel through the crystal it acquires some dispersion from it so that the minimum duration is stretched to about 60 fs [17]. By introducing a pair of prisms it is possible to compensate for the GVD simply by adding GVD with a negative sign, so that pulse durations of 20 fs can be realized inside the cavity. When we first set up the laser and aligned it, we mainly followed the instructions in ref. [19]. After all optical elements were fixed to the table in a rough alignment estimate, the fine tuning began. By looking at dim reflections of spontaneous emission off the prisms we finally got the laser to lase in cw mode, with output powers of 800 mW. By adjusting the cavity alignment we could make the laser operate in several different TEM laser modes.

In order to modelock the laser, we minimized the amount of prism glass the beam had to travel through, and to make use of the Kerr lens effect, we had to move 'curved mirror 2' a little towards the crystal. Prior to moving

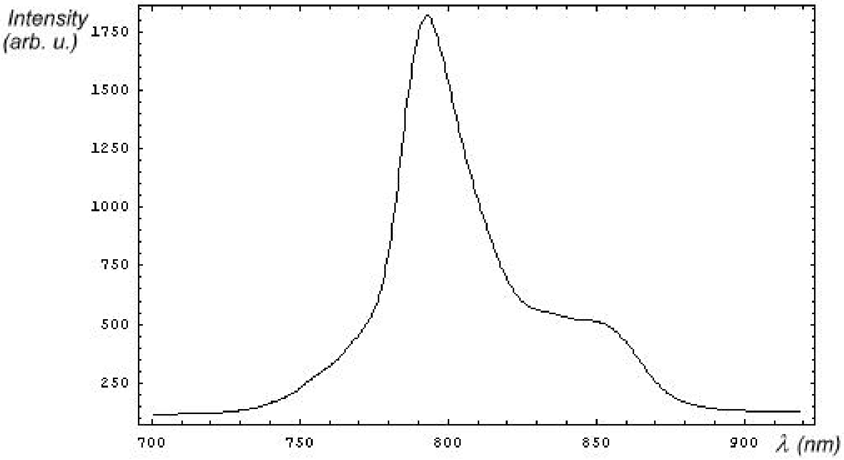

Figure 2.5: Typical oscillator spectrum

the mirror the cavity was optimized for cw lasing. After moving it, the cavity was optimal for a beam that gets an additional focussing from the crystal. Watching the output beam one could see that the cw mode with its Speckle pattern became unstable, an indication that the cw and the modelocked (ml) operation are competing. The modelocking was finally achieved by introducing an intensity fluctuation to the beam by giving a slight impulse to ‘Prism 1’. The ml laser beam was perfectly round and did not show the Speckle structure. We observed output powers of up to 700 mW in ml operation, but on an everyday basis we use it at about 400 mW with a bandwidth of 70 nm around the center wavelength of 800 nm. A typical spectrum can be seen in figure 2.5.

The oscillator turns out to be incredibly stable. No day–to–day alignment is necessary in general, one just has to put it into ml operation. This can be done by slightly moving the prism or just by knocking against the table. A first autocorrelation we took showed that pulses were 60 fs long and we calculated back that inside the oscillator the duration was about 20 fs, taking into account the dispersion of the 9.53 mm BK 7 output coupler. Substituting the end mirror with a special chirped mirror that compensates for GVD did not make the pulse shorter. The limiting factor inside the cavity is at least third–order dispersion, based on ref. [22], because the GVD can be compensated by the prism pair.

2.5 The Amplifier

Our amplifier system is a multipass chirped pulse amplifier (CPA) from KM Labs (KM Labs Model HAP–AMP) with high average output power. As we did not build it but bought it already completely set up, I will not go into detail and only describe the basics.

The femtosecond pulses from the oscillator with a few nanojoules energy at a repetition rate of 85 MHz enter the amplifier and first get temporally stretched ("chirped") by the stretcher which mainly consists of a grating that can separate the frequencies spatially. When they are brought back together again, the pulse has a duration of several hundred picoseconds. After that, the pulses (at p–polarization) go through a Pockels cell that picks out exactly one pulse per millisecond and turns its polarization to s, all other pulses during that millisecond are thrown away. This is done to match the repetition rate of the pump laser for the Ti:Sapphire amplifier crystal, which operates at 1 kHz.

It is a Nd:Yag laser from Quantronix at a wavelength of 532 nm that produces pulses of a few hundred nanoseconds duration and can reach average pump powers of up to 15 W.

The Ti:Sapphire crystal is inside a high–vacuum chamber. As a lot of energy is stored inside the crystal by the pump laser, the crystal is cooled by liquid nitrogen in order to maximize its gain efficiency (which is larger for lower temperatures) and to suppress thermal lensing. When the oscillator pulse that got picked by the Pockel cell propagates through the crystal, it leads to stimulated emission and gets amplified with a gain factor of about 10 per pass. After this first amplification, the pulse travels through a 3 μm pellicle that effectively broadens the bandwidth of the pulse by increasing the loss for the center frequencies. This means that the gain per pass through the amplifier is flatter than it would be without the pellicle. This process can be repeated in order to make use of all the stored energy inside the crystal. For this, the pulse is reflected back into the crystal at slightly different angles and gets amplified further until a gain saturation of about 10^6. In our setup, a pulse undergoes twelve of these passes through the crystal, the first eight of which go through the pellicle, before getting picked off by a mirror. The apparatus is called a multipass amplifier. The name CPA is due to the fact that the pulses get chirped first in the stretcher to longer durations and lower peak powers, so that the crystal does not get damaged, but also to increase the time where gain inside the crystal can be achieved [20, 24].

Finally, the amplified pulse is recompressed in the compressor which mainly consists of a pair of diffraction gratings that can put a negative dispersion to the pulse and thereby compensate for the chirp in the stretcher. It is even possible to compress the pulses to shorter durations than they had after the oscillator, simply because the grating compensates for the output coupler, thus making shorter pulse durations possible.

In everyday use the amplifier is run with a pump power of $11 - 12$ W and produces pulses of about 30 fs at an output power of $0.9 - 1.2$ W, which corresponds to a pulse energy of 1 mJ and peak powers of 30 GW or more. A typical pulse spectrum and its characteristic FROG trace (see following section) can be seen in figure 2.6.

2.6 Frequency–Resolved Optical Gating

Since the pulses in our experiment are only a few femtoseconds long, it is not easy to measure their actual duration or the shape of the electric field. In order to understand the effect of a given pulse in a reaction with a chemical, it is necessary to precisely know the shape of the pulse. Unfortunately no electronic device can respond fast enough to facilitate a measurement of the pulses over time. The fastest available photodiode has a rise time of hundreds of picoseconds and is therefore too slow. The only possibility to get access to the properties of the pulse is to measure it using itself, *i. e.* one has to use a nearly instantaneously responding nonlinear medium and a setup that allows for recovering the full electric field of the pulse.

Our first measurements to obtain the length of the oscillator pulses were made using an autocorrelator like it is shown in figure 2.6. It mainly works

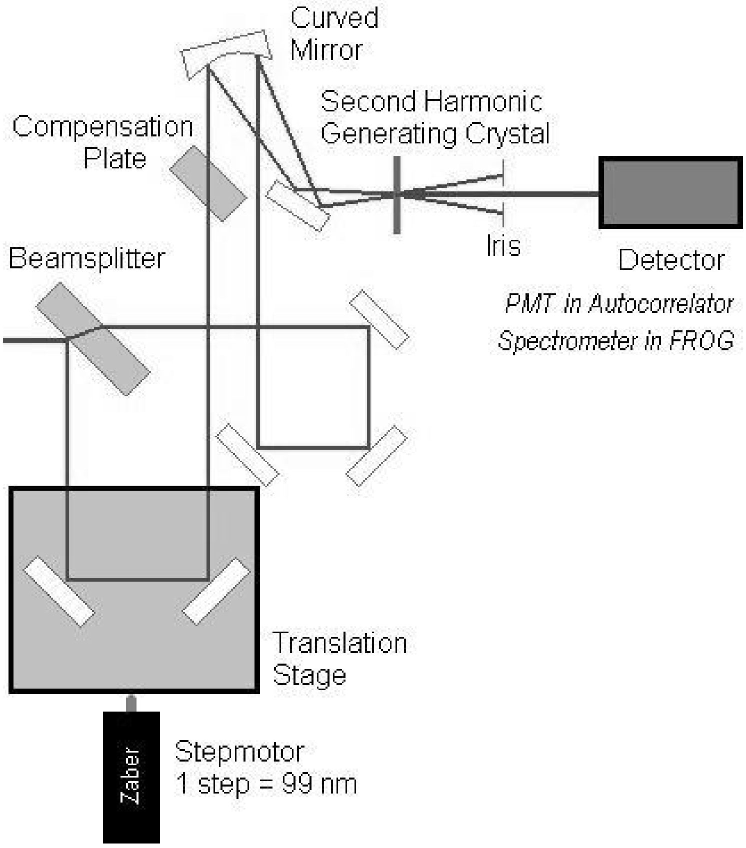

Figure 2.6: Setup for the autocorrelator and the FROG

like a Mach–Zehnder interferometer, although the beams are not recombined interferometrically. The imput beam is first split into two beams of equal intensities using a beam splitter. The length of one of the the two arms of the interferometer can be adjusted using two mirrors on a translation stage that can be moved using a stepper motor (one step equals 99 nm). By doing this it is possible to control the time delay between the two pulses in the two arms of the interferometer. The two beams are reflected so that they propagate parallel to each other and are finally focussed by a curved mirror to the same point inside a BBO (β–barium borate) crystal. The crystal is cut for type I phase–matching at 800 nm and therefore is suitable for second–harmonic generation. Both beams leave the crystal at the same angle they entered it, but they have contributions of frequency–doubled light afterwards. A compensation plate is introduced into the setup to match dispersion in both arms, because the beam that goes through the beam splitter gets a little chirp from the material and therefore is slightly longer. The plate, made of the same material as the beam splitter, stretches the beam in the other arm in the same way so that both beams are still equal at the crystal. However, a calculation showed us that for a 20 fs pulse, the stretching does not add more than half a femtosecond.

Each of the two beams with wave vectors $\mathbf{k}_1$ and $\mathbf{k}_2$ generates second–harmonic with $2\mathbf{k}_1$ and $2\mathbf{k}_2$ inside the crystal, so that two outcoming frequency–doubled beams can be observed behind the crystal for all delays. By moving the stepper motor (one step actually means 198 nm of delay, which corresponds to 0.67 fs) the time delay τ between the two pulses at the crystal is varied. It can be less than a pulse duration, *i. e.* the two pulses overlap not only spatially, but also temporally at the focus inside the crystal. Then both beams can contribute to the creation of frequency–doubled light simultaneously, which results in the generation of a third blue beam with wave vector $\mathbf{k}_1 + \mathbf{k}_2$. Due to conservation of momentum this light will leave the crystal exactly between the other two beams. The fundamental beams are blocked by an iris, so that only light can reach the detector that is created by both beams, *i. e.* at the step motor position where the pulses overlap inside the crystal.

The detector of the autocorrelator is a photomultiplier tube (PMT), and one simply measures the intensity of the frequency–doubled light for different time delays. Unfortunately, the intensity autocorrelation does not lead unambiguously to the intensity as a function of time [2], so we only gain information about the pulse in the time domain. The internal structure, *i. e.* the phase and $I(\omega)$, is lost by integrating over all frequency components of the second–harmonic in the PMT. In order to acquire the full electric field, we had to modify the apparatus. The PMT was replaced by an Ocean Optics Spectrometer (range $\approx 300 - 500$ nm) in order to build a FROG (Frequency–resolved optical gating)[3], *i. e.* the signal was spectrally resolved.

With the spectrometer it is possible to collect information about the contributing frequencies in the doubling process, too, by simply spectrally resolving the signal beam of the autocorrelation, that is why one often refers to the "time–frequency" domain [25]. The result of a FROG measurement therefore is a $2D$–contour spectrogram ("FROG trace") depending on the frequency or wavelength and the delay time. The signal field of our FROG takes the form

$$E_{signal}(t,\tau) \sim E(t) \cdot E(t-\tau) \tag{2.23}$$

---

[2] *e. g.* pulses with negative and positive chirp have the same autocorrelation; in order to get information of the pulse duration, a pulse shape has to be assumed in advance

[3] The name "optical gating" has been used because the first apparatus to use a similiar setup just detected one beam that traversed a nonlinear crystal that was less absorbed in the presence of the other pulse, *i. e.* acted as a gate function [25]–[28]

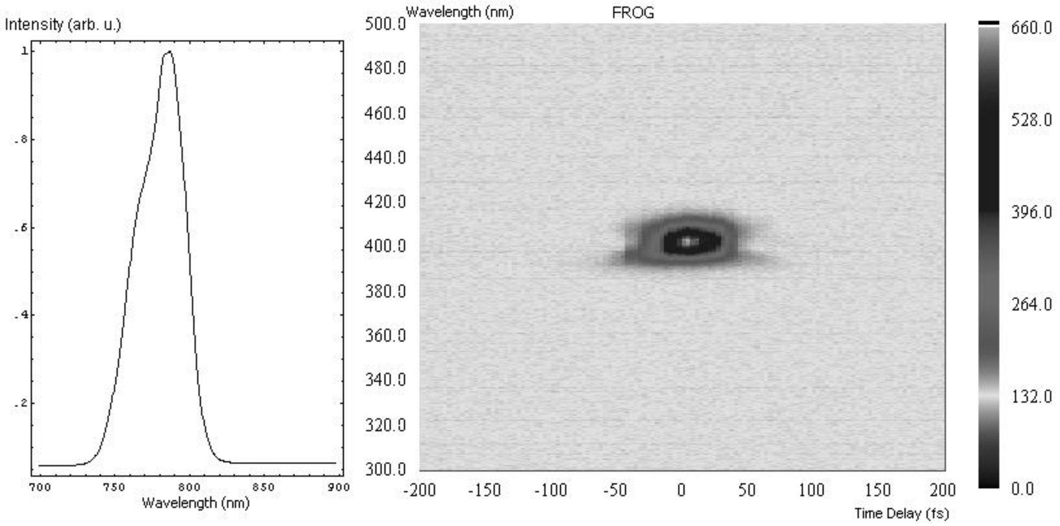

Figure 2.7: Typical FROG trace and corresponding spectrum of a pulse from the amplifier

so that its magnitude in the FROG trace is given by the squared Fourier transform of the signal field [28]:

$$I_{FROG}(\omega, \tau) = \left| \int_{-\infty}^{\infty} E_{signal}(t, \tau) \exp(-i\omega t) dt \right|^2 \tag{2.24}$$

The FROG traces were recorded with a LabView program from KM Labs that I modified so that it works with the Zaber motor and our spectrometer. The program comprises an algorithm to subtract background noise and a reconstruction algorithm to retrieve the electric field of the input pulse from the FROG trace[4]. It mainly starts from an initial guess and then simulates FROG traces that satisfy the constraints (2.23) and (2.24), compares them to the recorded one and minimizes the error. The reconstructed electric fields

---

[4] for a description of the algorithm, look into ref. [28]

are in general unambigous over a large range of pulse durations, frequencies and complexities, and the method is found to be “general, robust, accurate and rigorous” [28]. A typical FROG trace and the corresponding spectrum of a 31 fs pulse from the amplifier with a bandwidth of 37 nm around a central wavelength of 785 nm is shown in figure 2.7. One can also see that an integration of $I_{Frog}(\omega, \tau)$ over all delays τ just gives the autoconvolution $I(\omega)$ of the frequency–doubled light, while integration over ω reproduces the ordinary autocorrelation $I(\tau)$ that we got with the PMT. However, the FROG trace is always symmetric around $\tau = 0$, so that one actually cannot distinguish between positive and negative chirps of the pulse. This disadvantage of the second–harmonic FROG can be overcome by other designs (*e. g.* third–harmonic FROGs). While these FROGs do not feature the time ambiguity, they are more complicated to construct and require higher intensities. The ambiguity can also be resolved by inserting a known piece of material in front of the FROG and measuring the changes in the pulse characteristics.

Chapter 3

The Time–of–Flight Mass Spectrometer

One major part of the project was to design, build and test the vacuum system. In order to faciliate the discussion, a basic mathematical description is provided.

3.1 Vacuum Equations

Our turbo pump has a pumping speed of $\frac{dV}{dt} = 56$ l/s at the inlet. Its "throughput" Q is given by

$$Q = P \cdot \frac{dV}{dt} \tag{3.1}$$

where P is the pressure; the units of Q are torr·l/s. Since the system should mainly be realized using metal tubes, one has to know how these behave when pumped out. Their throughput is defined as

$$Q = k_B T \frac{dN}{dt} = (P_1 - P_2)C \tag{3.2}$$

with P_2 is the pressure at the end of the tube where the gas streams out. The new quantity C is the tube's "conductance", which is a measure of a tube's capacity for transmitting gas.

The conductance of a tube does not only depend on geometrical factors, but also on the density of the gas that is inside. The important quantities are the mean free path λ of the gas and the Knudsen number $K_n = \frac{\lambda}{a}$, where a is a characteristic dimension of the tube (either the length or diameter, the smaller one). If K_n is smaller than 0.01 the molecules undergo many of collisions before reaching a wall. This regime is known as "viscous flow". On the other hand, if K_n is larger than 1, molecules rarely collide and do not interact. This is known as the "molecular flow" regime. In the transition region (Knudsen region) between the two ($0.01 < K_n < 1$), the description is more difficult. Only semi–empirical formulas can be used as a description [30]. In the viscous flow region, the conductance depends both on the average pressure P_{AV} and the viscosity η of the gas. For a cylindrical tube it becomes (tube diameter d):

$$C_{vf} = \frac{P_{AV} \pi d^4}{128 \eta L} \tag{3.3}$$

In the molecular flow regime, there is no dependence on the pressure, and the conductance takes the form:

$$C_{mf} = \frac{\pi d^3}{12L} \cdot \bar{v} = \frac{\pi d^3}{12L} \sqrt{\frac{8 k_B T}{\pi m}} \tag{3.4}$$

with the mass m of the molecule.

From these formulas, one can see that tubes with different characteristic lengths do not have the same ability to transmit gas. Thus, one can combine tubes of different diameters to create regions with different pressures in the setup without having to use several pumps. A chamber with a tube connecting to a high vacuum region and another connection to a low vacuum region will eventually be in equilibrium at an intermediate pressure that is mainly governed by the conductances of the two tubes. Having several connected regions that are at different pressures in equilibrium is known as “differential pumping”. In a region with a liquid chemical and no other gas the pressure is the vapor pressure of the substance, if there is no pump that removes the molecules away. When there is a small connection to another chamber that is at vacuum, we see from equation (3.2) that the throughput is governed by the vapor pressure and the conductance of the connection. The vacuum chamber will fill with molecules and get to the vapor pressure as well, unless it has an opening to another chamber at even lower pressure. In the case where that low pressure is held constant by a pump, there will finally be an equilibrium pressure in the middle chamber, exactly when the two throughputs cancel each other, *i. e.* as many particles as enter the middle chamber also leave it in the same time, thus “differential pumping” is achieved [29].

3.2 Molecular Beam

To maximize the ionization signal, it is desirable that as many particles as possible get into the laser beam focus. However, the total amount of molecules entering the chamber should be kept low, because otherwise the vacuum would decrease. This can be realized by letting the molecules enter the vacuum chamber through a narrow nozzle, where the ratio of length to diameter should exceed 10 in order to achieve a reasonable collimation [29].

When the gas from a viscous flow region expands into vacuum with negligible background pressure compared to the other end of the narrow and long nozzle, the molecules will undergo many collisions and only those which have a velocity component parallel to the tube will make it through the nozzle, resulting in a narrower velocity distribution. Since the temperature and the speed of sound depend on the width of the velocity distribution, both will drop, and the Mach number increases steadily. At the point where it turns larger than one, the flow becomes supersonic. When the molecular flow region is reached, there is hardly any more collisions and the temperature is kept. The Mach number "$MACH$" can be calculated using the formula from ref. [31]:

$$\frac{P_{low}}{P_{high}} = (1 - \frac{\gamma - 1}{2} MACH^2)^{-1/(\gamma-1)} \tag{3.5}$$

which follows from the ideal gas equations (γ is the adiabatic exponent), although one has to say that an ideal gas and continuum flow, especially in the Knudsen region, are very optimistic assumptions.

The interpretation of the experiments is easier if most of the molecules are in the vibrational ground state. This shall be realized by a supersonic expansion. A small capillary leads to a withdrawal of energy from certain degrees of freedom due to inelastic collisions that transfer energy from internal degrees of freedom to directed motion, which means that the vibrational modes are by far less excited than they would normally be at room temperature (the temperature of the vibrational modes is smaller than the kinetic temperature). Therefore, clearly a supersonic beam is desirable, but in our apparatus, we have no unambiguous confirmation for it yet.

3.3 The Interaction Cube

Since our laser beam is supposed to ionize molecules, I had to build a chamber where the light can interact with a molecular beam. The basic framework consists of an aluminum cube of 7.5 mm side length, that has three tubes of diameter 3.8 mm bored through it which are centered on each of the 6 sides of the cube (similiar designs in [34, 35]). This is a standard that allows for connecting 6 KF40 vacuum nipples or flanges to the cube. In order to make a molecular beam, we decided to use a small syringe fiber of inner diameter 20 μm that should reach into the cube. Furthermore, a setup was necessary for imaging the nozzle and to position the nozzle optimally.

The syringes we use are from Western Analytical (outer diameter of 375 μm) and World Precision Instruments (O.D. 80 μm). These very small fibers are too sensitive to move them unprotected, so they are glued with special vacuum epoxy into a glass capillary (later steel to avoid charging) of O.D. $\frac{1}{4}''$. The mechanical feedthrough into the vacuum chamber is realized using a bored–through UltraTorr–fitting from Swagelok that is welded onto a KF40 steel flange. The feedthrough is constructed in such a way that the glass capillary can slide in and out of the chamber without breaking vacuum. On its other end, the capillary goes into a bored–through UltraTorr reducer with a steel tube of O.D. $\frac{3}{8}''$ and an I.D. larger than $\frac{1}{4}''$, so that the glass can also move into the steel tube without breaking the seal. The steel tube is connected to a special 3D translation stage that I built. If the UltraTorr at the steel tube is tightened harder than the one on the chamber, the glass will move with the steel tube, so that the nozzle position inside the chamber can be controlled by moving the translation stage (see figure 3.1a).

The interaction region where the molecular beam meets the laser focus lies between two steel plates of diameter 3.75 mm, which act as capacitor. The top plate has a small hole of diameter 1 mm at its center, through which the molecules will be able to escape the capacitor after they got ionized. Each plate has four holes close to its edge, through which the plates are held in place by four threaded 832 nylon rods from Microplastics. By using eight plastic nuts to sandwich each plate, one has a convenient way to change the distance of the plates as well as to control whether they are parallel or not. In addition, they are perfectly insulated from each other. The four nylon rods have to be attached to the bottom of the cube, which is realized by a special solid O–ring holder that is tapped for the rod. Close to its center, it has two holes for the wires that supply the voltage to the plates.

The first design for the electrical feedthrough to the plates was an aluminum flange with two holes, into which two wires in a ceramic were glued. Several leak problems in vacuum compatibility tests were tracked down to the ceramic being too porous. The second version, just copper wire glued directly into the holes, worked well until the vacuum chamber was baked for the first time to get rid of adsorbed molecules on the inside surfaces of the cube. After that leak problems were present again. Further tests showed that the glue (Loctite Hysol 1C epoxi–patch) loses its sealing ability above 100°C, which was also confirmed by graduate students from the Francium experiment next door. The final solution is a hollowed KF40 stub with flattened sides to which

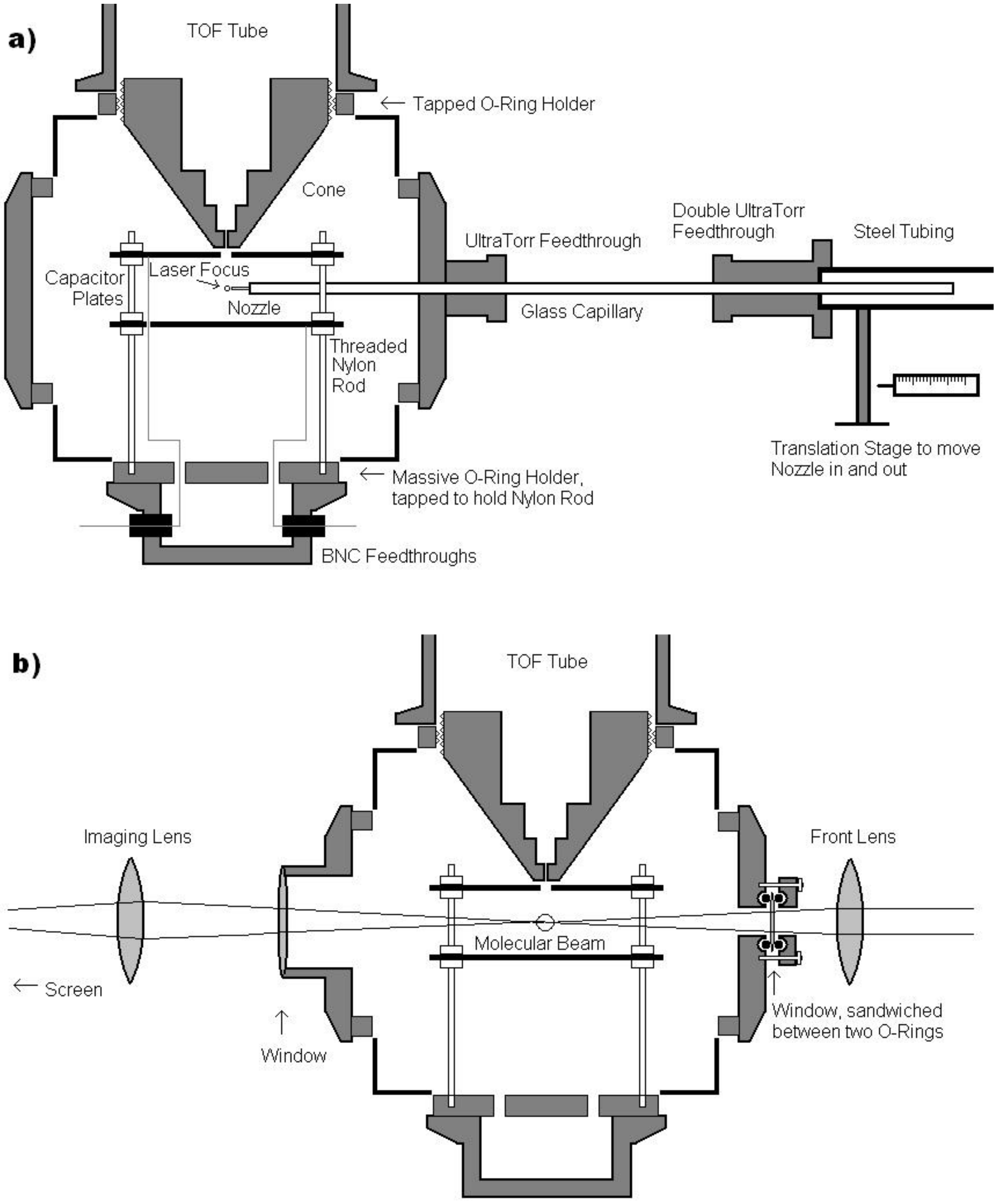

Figure 3.1: The interaction region inside the cube, seen from the incident direction of a) the laser; b) the molecular beam

two BNC vacuum feedthroughs have been connected. Inside, two insulated copper wires have been soldered to them, which run through the solid O–ring holder to the field plates, where they are attached by a tiny screw. The wire for the top plate actually goes through a small hole in the bottom one, but as the wire is insulated, no shorting problems arise.

By applying a positive voltage to the bottom plate and fixing the top plate to ground, cations get accelerated upwards and can get out of the capacitor via the hole. After that, they travel through an aluminum cone as can be seen in figure 3.1, that has three purposes: first it acts as an additional aperture after the cone, second it shields the voltage of the top plate (if different from ground) from the region above it, and third, it allows us to create a system of differential pumping. In order to control the first one, the cone is threaded on its outside and held by a tapped O–ring holder. Thus, it is possible to alter the distance to the top plate of the capacitor. The last one is the most important one, because the molecular beam of course raises the pressure in the chamber, while our detector system (see 3.5) requires high vacuum.

The cone has a flat point with a hole of diameter 1 mm (later changed to 1.2 mm) and a length of 2 mm. In order to match the throughput of the nozzle and the cone, we first make an estimate for the pressures involved. Behind the nozzle, the vapor pressure of our chemical dominates (*e. g.* 760 torr for air, 100 torr for benzene at room temperature). In the detector region a pressure of 10^{-7} torr regime is desired and is reachable with our turbo pump, while inside the cube a pressure of 10^{-4} torr should be kept, where the mean free path is a few tens of centimeters, so the molecular beam does not encounter too many collisions prior to the interaction region. For these values, the throughput of the cone is $6.0 \cdot 10^{-6} \frac{torr\ l}{s}$ ($2.1 \cdot 10^{14}$ particles per second), where one makes use of formulas (3.2) and (3.4). This has to equal the throughput of the nozzle. Unfortunately, the vapor pressure is so high that the Knudsen region lies inside the nozzle. Therefore, it is not clear whether viscous or molecular flow is dominant. Using formulas (3.3) and (3.4), one sees that the conductance is about $0.5 - 5$ times (for $100 - 760$ torr) higher assuming pure viscous flow than it is when pure molecular flow is assumed. Because of the small diameter of $20 \mu m$, the beam becomes supersonic after a very short distance, which is why we assume molecular flow over approximately the whole length. For air we find that the throughputs are matched if the syringe has a length of 6 cm. The outcoming molecular beam should then have a Mach number of over 100, according to formula (3.5), although the continuous flow and pure ideal gas assumptions might not hold after a certain length.

Although these calculations do provide a rough estimate of the pressures involved and the appropriate sizes for the components involved, they do not include some relevant aspects of the experiment. Outgassing inside the chamber is a severe problem because the throughput of the cone is so small and therefore it takes long to pump it out. This can be overcome by baking the cube. Though it is possible to reach the desired pressure regime after baking without the molecular beam, we did not achieve it with atmosphere as backing pressure for the syringe. The pressure then exceeds 10^{-4} torr in the interaction region. Also, the turbo pump can get into the 10^{-7} torr regime, but not when the whole vacuum system is connected to it. The day–to–day pressure above the cone is about $2 - 6 \cdot 10^{-6}$ torr.

Since we tried to keep the laser at a height of $4''$ above the table in our setup, I machined the cube assembly in such a way that the laser beam can enter the cube through a thin anti–reflection coated Sapphire window of thickness 250 μm from CVI whose center is at a height of $4''$ above the table. The window is thin because one wants to avoid additional dispersion for the pulse. The first optical feedthrough consisted of a steel flange with a hole on which I glued the window. When it came to baking the chamber, the glue proved to be inappropriate for the window, too, because a leak formed. The glue–free version can be seen in figure 3.1b. The hole in the flange is surrounded by a groove that holds an O–ring onto which the window is laid. A metal ring with another O–ring is tightened onto the flange with screws so that the window gets sandwiched between the O–rings. This version turned out to be very good and seals well, especially because the vacuum itself presses the window onto the O–ring and seals it.

The laser beam leaves the chamber through a commercial viewport constructed from ordinary thick glass. After this window, a lens makes it possible to image the interaction region onto a screen. This is very convenient in order to find the overlap of various axes: in fact all three axes have to be optimized for obtaining a signal, because the position of the hole in the capacitor plate, the laser beam focus and the molecular beam height have to overlap. Two of them can be simplified by the imaging lens. Without a laser beam and a focussing lens before the chamber one can simply take a flashlight and image the nozzle and a thin wire that is stuck through the field plate hole onto the screen and thereby produce a cross hair (see figure 3.4 later), so that finding a signal can be reduced to positioning the image of the focus to the place of the cross hair.

3.4 Microchannel Plates

A microchannel plate (MCP) consists of millions of narrow glass capillaries fused together and finally cut into a thin plate. When a charged particle (or an x–ray photon or neutron) enters such a channel, it can emit several electrons from the channel wall when it hits it, and a voltage across the plate accelerates these electrons towards the other MCP side. As the channels are not perpendicular to the surface but slightly tilted, this happens many times before the back of the MCP is reached and thus, an avalanche effect is caused that leads to a gain of about 10^4 at an acceleration voltage of 1000 V across the plate. Furthermore, the channels confine the electrons and enable spatial resolution, if needed (we actually do not need spatial resolution). The high temporal resolution make them useful for time–of–flight spectroscopy [32].

In order to increase the gain, one can combine several MCPs behind each other. Two impedance–matched (*i. e.* with the same resistance) MCPs with opposite channel tilt are called "Chevron" assembly, and can reach a gain of 10^8.

The MCPs we have are a Chevron assembly (Del Mar Ventures, Model MCP 24A/2) with channels of 10 μm diameter, a tilt angle of 5°, a total diameter of one inch and an active area of at least [5] 18.5 mm diameter, an open area ratio of 55% and a thickness per plate of 430 μm.

3.5 The Detector

When the ions are produced by the laser beam they leave the cube via the plate hole, they enter the time–of–flight tube which consists of a field–free region and the detector. The latter one can be seen in figure 3.2. Because we wanted to keep everything as compact as possible and the volume that has to be pumped out very small, we wanted to keep everything in a standard vacuum tube, so we developed an appropriate design and realized the detector inside a KF50 nipple. Again, nylon rods from Microplastics were used to keep it in place.

The detector consists of a steel KF50 blank flange from Trinos Vacuum, into which I machined two BNC vacuum feedthroughs for the MCP backplate and the anode that detects the signal. Furthermore, an SHV feedthrough was welded onto it for the MCP front voltage. Underneath the flange, a massive, solid O–ring holder of 1$''$ thickness is placed. There are three holes drilled into it, so that the electrical connections can reach through, and also three soldering holes (not in figure 3.2) from the side to enable connecting the wires to the feedthrough. The main part of the O–ring holder has a diameter of 4.8 cm and reaches into the KF50 nipple. Close to its edges, there are four tapped 440 holes with threaded nylon rod. All other parts except the MCPs have four

---

[5] the channel pattern is not exactly round, so there is a minimum radius

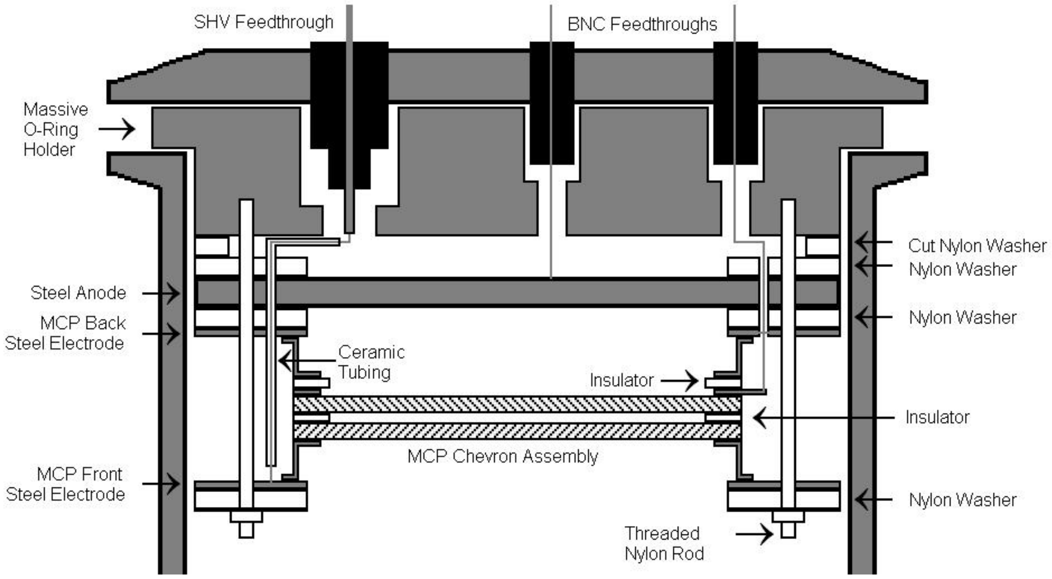

Figure 3.2: Cross section of the detector system of the TOF spectrometer

holes and are simply stacked up. Thus, the whole assembly is very robust. The first layer is a nylon washer with channels cut for the MCP wires to go to the edge of the assembly (see figure 3.2), then an ordinary washer to insulate the following anode, which is made out of a $\frac{1}{8}''$ stainless steel plate. We considered making a conical anode, like it is used in electron TOF spectrometers, to match the impedance, but came to the conclusion that this is not necessary for ions, as the time resolution of a simple plate should be sufficient. On top of the anode there is another nylon washer and then the back electrode consisting of a very thin steel ring with a center hole of diameter $1''$, the area of the MCPs. Del Mar Ventures produces the MCP Chevron assembly glued into holder consisting of a Z–shaped metal ring, an insulating ring, a metal ring (connection for the backplate voltage), the MCPs and another Z–shaped metal ring (for the frontplate voltage). The design allows for placing the MCPs between the nylon rod, placing another thin electrode and a nylon washer onto it and tightening the whole assembly with plastic nuts, so that the MCPs stay in place and have good contact to the electrodes. The wire to the front plate is guided by a ceramic tube to make sure the high voltage cannot short out somewhere.

3.6 Complete Vacuum Setup

A view of the total vacuum system can be seen in figure 3.3. The molecular beam enters the chamber through the nozzle and proceeds to the interaction region in the middle of the cube underneath the field plate hole. The cations get accelerated towards the hole and escape through it, pass the cone and enter the time–of–flight tube, where they first see a field–free region of $\approx$ 26 cm length until they reach the grounded wire mesh. The wire mesh has an open area of about 44%. We measured its transmission optically. After the mesh the particles see the negative high voltage of the MCP front, are accelerated towards it and finally cause a cascade of electrons that hits the anode and can be seen on the oscilloscope.

The actual distances between MCPs and mesh, mesh and capacitor plate, and plate and laser focus do no affect the TOF spectrum pattern in a significant way, they simply shift the peaks together. The distance between laser focus and top plate changes with the beam height anyways. As all particles are produced at the same time, travel the same distances and see the same acceleration voltages, the time for different peaks on the scope is directly related to their mass (their ratio of charge to mass, to be exact) via the relation:

$$\frac{t_1}{t_2} = \frac{m_1^2 q_2^2}{m_2^2 q_1^2} \tag{3.6}$$

This equation is only true if they all have the same kinetic energy when they are created by the laser pulse. Formula (3.6) can be used for the calibration of a spectrum if two peaks can be easily identified. The length of the TOF also is sufficiently small so that there is no overlap of signal from different laser pulses. The repetition rate of our amplifier is 1 kHz, *i. e.* one pulse each millisecond, while in the experiment heavy ions like benzene (78 atomic mass units) arrive after less than 100 μs, while lighter ones arrive earlier.

In the experiment it is desirable to have the possibility of easily changing the molecular sample while still achieving the highest purities. We realized this by the design shown in figure 3.3: a test tube that was made for us by the glass blower of the chemistry department. It is connected with an UltraTorr fitting to the vacuum system and can be removed easily. In order to get a pure molecular beam, we make use of “freezepump cycling”. With both the freezepump and the beam valve closed, one first pours the old substance out of the test tube and cleans it. Once the sample holder is replaced, we close the turbo breath valve and open the freezepump and the beam valve, so that all remaining molecules from the previous sample are evacuated. Also molecules on the inside of the tubes are pumped out by the roughing pump. The freezepump valve is closed again and the new chemical is poured into the

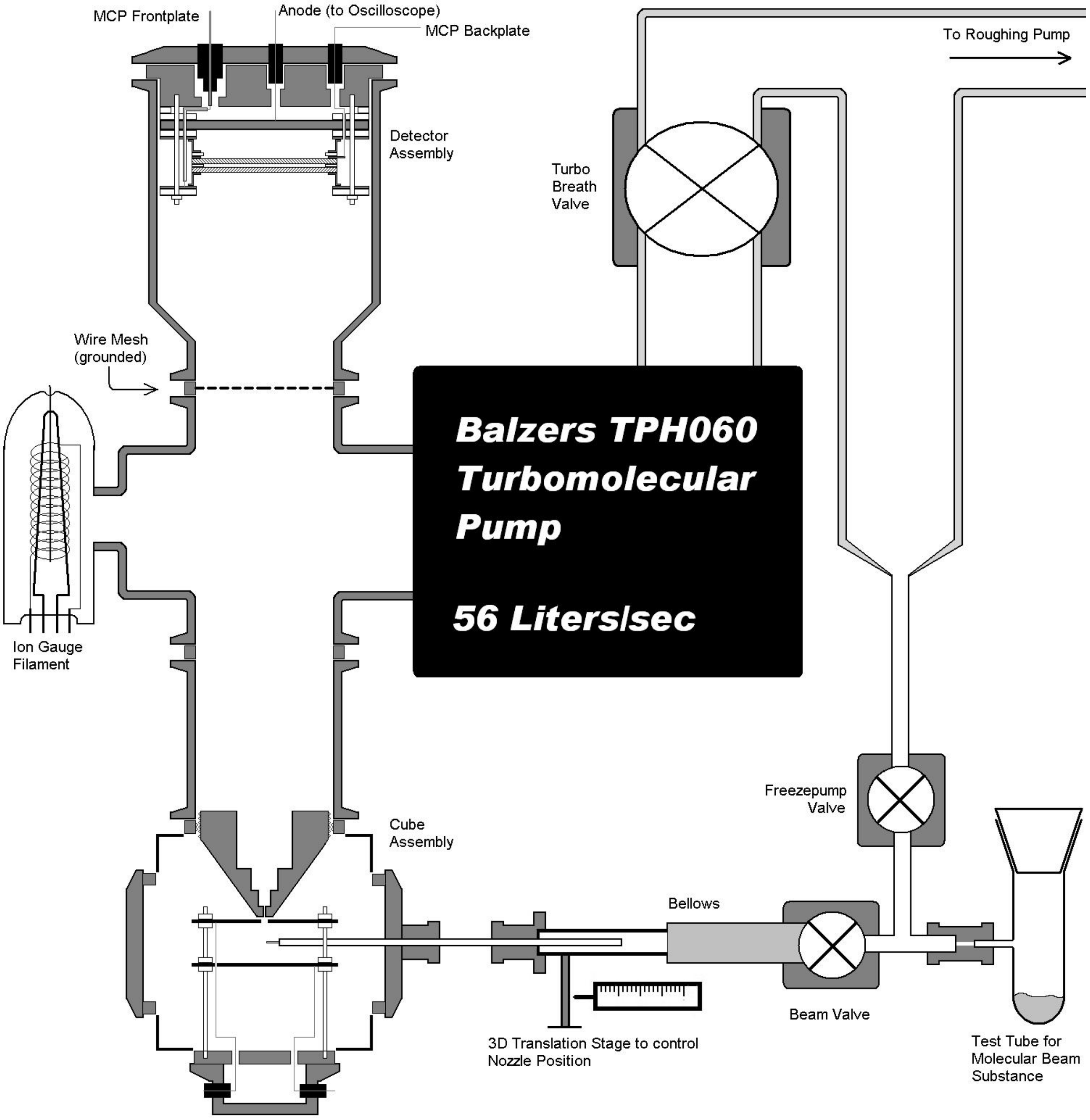

Figure 3.3: Complete setup of the vacuum system

test tube. Then, the test tube is dunked into a styrofoam cup with liquid nitrogen. The substance will freeze, while most of the other gas (nitrogen, oxygen, hydrogen) that is in there will not. Unfortunately water will not get pumped out, but we can look for it at mass 18 amu, where there is nothing else. Opening the freezepump valve will pump most of it away, especially when the melting point of the substance is high and it will therefore immediately freeze, so that other gas components in there cannot reach their freezing point. After closing the valve again the substance will melt, as well as other substances that nevertheless froze, but that will now vaporize to a large extent. By repeating the freezepump cycle several times the amount of typical air molecules can be minimized, although it is hard to get rid of some components that have a high freezing point, namely water. After enough cycles the freezepump valve is closed for good, the breath of the turbo is opened again, and while the chemical is melting the pressure in the test tube will rise to the characteristic vapor pressure and the molecular beam increases to its final intensity. Another convenient feature of the molecular beam setup is given by the beam valve. When the substance is slowly melting after the freezepump cycle, it passes through all temperatures from 77 K (liquid nitrogen) to room temperature. The beam valve allows us to choose any vapor pressure in that temperature region. The bellows and tubes between the valve and the nozzle can be regarded as an infinite reservoir in regard to the throughput of the nozzle. Thus, the pressure behind the nozzle can be easily controlled.

3.7 Pump Probe Setup

In order to study the internal dynamics of the molecules and to distinguish between neutral and ionizing dissociation we built a Mach–Zehnder interferometer to have two separate pulses cross at the focus inside the interaction cube. The setup can be seen in figure 3.4. The beam from the amplifier hits a beamsplitter and is divided into the pump (transmitted) and probe (reflected) beam.

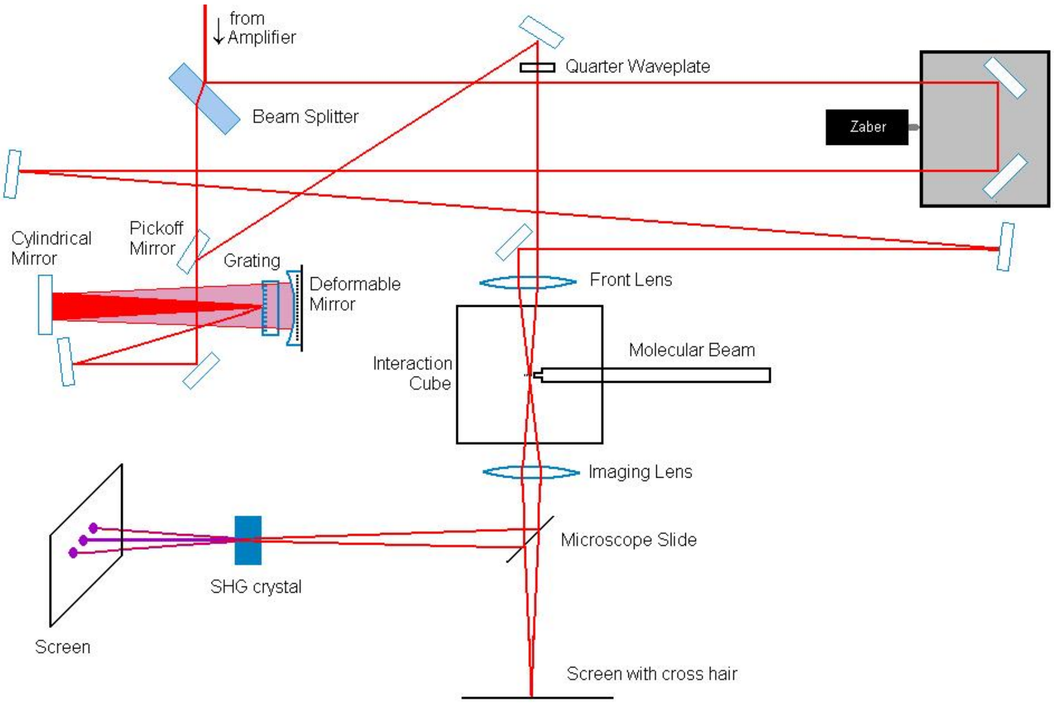

Figure 3.4: Pump probe setup for the laser incidence into the vacuum chamber; the laser beam enters a Mach–Zehnder interferometer with the deformable mirror pulse shaper in one arm and the stepper motor in the other one to control the time delay

In a deformable mirror pulse shaper designed by David Cardoza, the beam hits a grating and therefore acquires a spatial chirp, *i. e.* the different frequencies are spread to different positions. A cylindrical mirror is used to collimate parallel incidence of the different frequency components onto the deformable mirror, a gold–coated pellicle. Behind the mirror, there are twenty vertical metal pins to which high voltage can be applied. This leads to a deformation of the mirror because the pin and the mirror act like a capacitor and we get an attractive force on the mirror. The active optical length that certain frequencies have to travel until they get reflected can be controlled by this assembly, which means that we are able to control the arrival time of the different frequency components in the pulse and therefore the pulse shape. Since there are twenty pins with 256 voltages for each, we can theoretically shape the pulse in 256^{20} (more than 10^{48}) ways. In learning control pulse shaping experiments a genetic algorithm is used to control and alter the voltages on the pins in order to increase a certain signal. Using different techniques [38, 39] to decide whether a pulse shape is good or bad the algorithm can stepwise optimize the desired signal without having information about the Hamiltonian of the system, thus one speaks of learning control. The apparatus presented in this thesis will eventually be used for genetic algorithm learning control experiments like in ref. [40, 41, 44].

After hitting the deformable mirror the pulse travels through the pulse shaper again at a slightly lower height and gets picked off by a pickoff mirror that sends it to another mirror and from there onto the front lens before entering the chamber. A waveplate can be put after the last mirror to control the polarization of the pump beam (see section 5.3).

The probe beam just goes through a delay line (see figure 3.4) that has exactly the same length that the pump has to travel before entering the chamber (more than three meters). The last mirror sends the probe beam parallel to the pump beam onto the front lens so that they are focussed to the same point into the chamber. As our pulses are just $30 - 100$ fs long it is not easy to make sure that they both arrive at the focus at the same time. In order to control this we have another Zaber step motor in the delay line that can control the time delay between the pulses and that enables us to move the probe beam through the pump beam, *i. e.* to control whether the probe or pump arrive first or whether both overlap ("time–zero"). Time zero is found by refocussing the beams with the imaging lens and creating an image of the focus outside of the chamber. The reflection of a microscope slide is sent to a KDP doubling crystal to generate second–harmonic light. Like in the FROG, the temporal and spatial overlap of the two beams can be recognized by three instead of just two frequency–doubled beams that leave the crystal. This overlap inside the crystal therefore is an indication for overlap inside the chamber.

As our ultrashort beam is composed out of a broad bandwidth of wavelengths one has to worry whether all these components all have the same focal point. The differences in focal length and Rayleigh range for a planoconvex $BK\ 7$ lens that has a focal length of 10 cm for 532 nm are given in table 3.1. The indices of refraction have been taken from the Melles–Griot catalogue, the numbers have been calculated using formulas from ref. [1]. The measured beam waist is 2 mm before the lens and we have almost zero curvature.

λ (nm)	$n(\lambda)$	$f(\lambda)$ (cm)	$w(\lambda, f)$ (μm)	$z_0(\lambda, f)$ (μm)
532	1.51509	10.000	10.073	506
786	1.51106	10.079	12.61	639
821	1.51.037	10.093	13.19	670

Table 3.1: Focal length, beam waist and Rayleigh range of the front lens for different wavelengths

One can see that the difference in focal length in the frequency regime around 800 nm is about 150 μm, while twice the Rayleigh range is almost ten times this number. Therefore, although the focus will be at different points, the regions of biggest intensity will overlap for all frequencies. We also bought an achromatic lens that reduces spherical aberrations by a factor of ten, so that there is no displacement of the foci of the two beams when they hit the lens parallel, but not necessarily symmetric around the axis of the lens.

Chapter 4

First Results

4.1 Air Measurements

After everything was assembled, first measurements could be taken. Several LabView programs were written and the Digital Oscilloscope (Tektronix 2430A) was connected to the computer via a GPIB connection. At first, we simply let the laser beam into the chamber without a molecular beam. We ionized the background gas in the chamber that was at a higher pressure than it was with the molecular beam. The raw data can be seen in figure 4.1, where 100 traces have been downloaded from the oscilloscope and averaged on the computer. This data was taken with -1800 V at the front and -30 V at the back plate of the MCPs, $+75$ V at the bottom capacitor plate and a grounded top plate. The laser pulse was not fully compressed and had a duration of 54 fs. The plots a (top) to c (bottom) correspond to pulse energies of a)50 μ J (ND1), b)110 μJ (ND0.5) and c)350 μJ or intensities of $1.7 \cdot 10^{14}$ Wcm^{-2}, $3.8 \cdot 10^{14}$ Wcm^{-2} and $1.2 \cdot 10^{15}$ Wcm^{-2} in the focus.

The three plots show the actual data array from the oscilloscope, which

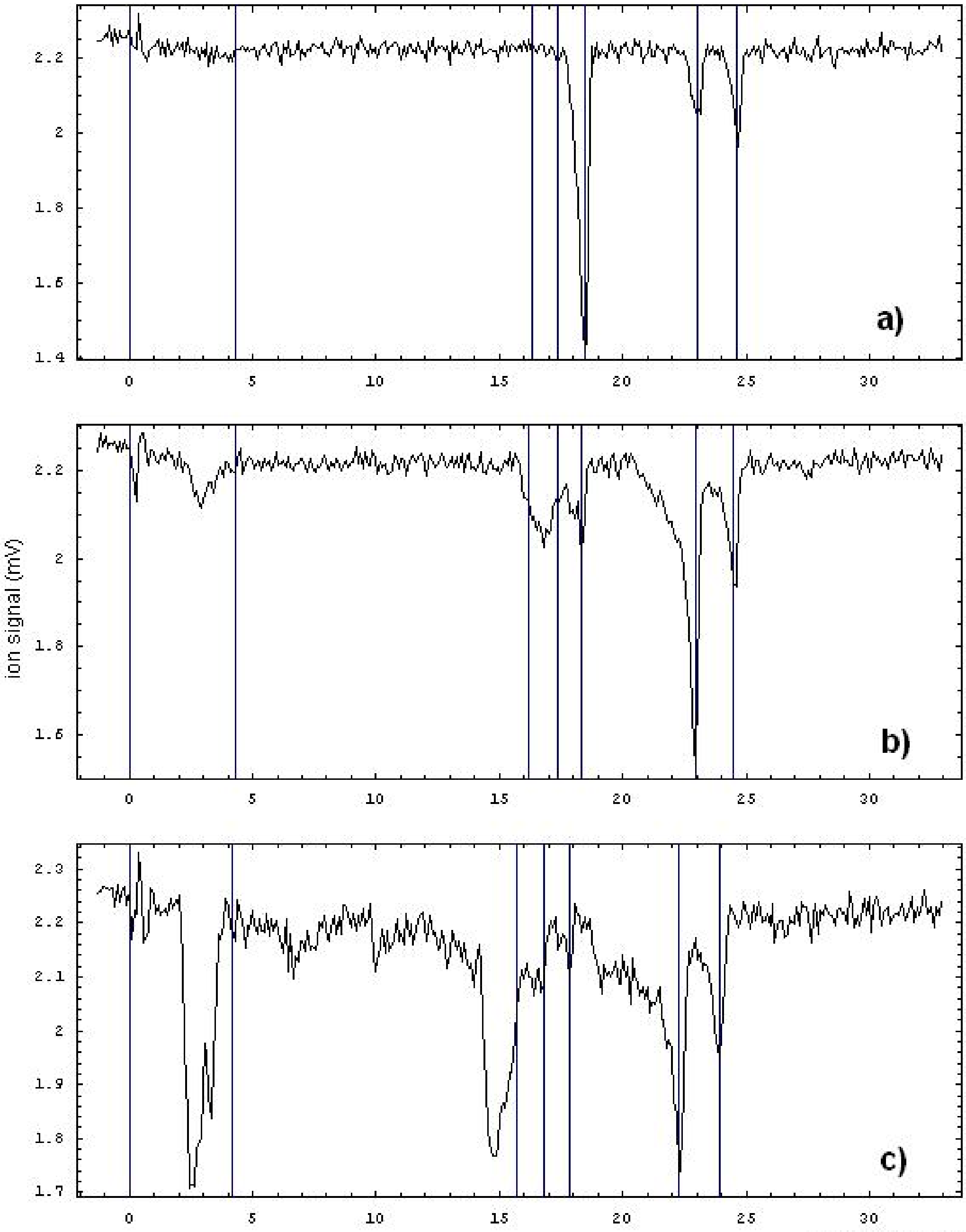

Figure 4.1: Oscilloscope traces for the ionization of air at intensities of a)$1.7 \cdot 10^{14}$ Wcm^{-2}, b)$3.8 \cdot 10^{14}$ Wcm^{-2} and c)$1.2 \cdot 10^{15}$ Wcm^{-2}; The bars correspond to the trigger position and arrival times of ions with a mass of 1, 14, 16, 18, 28 and 32 amu

is triggered by a fast photodiode behind the window of the interaction that looks at the image of the focus in the chamber. As the trigger position is set to be in the middle of the downloaded trace, only the data points 500 to 850 (which corresponds to the 35 μs after the laser pulse ionized the molecules) from 1024 are plotted. Assuming the N_2^+ peak can be easily identified, the scale can be calibrated. The grid lines in the plot show the position where peaks should appear that resemble time zero and masses of 1, 14, 16, 18, 28 and 32 atomic mass units, because we expected to see hydrogen and water as well as nitrogen and oxygen molecules and atoms at high intensities.

The result for the lowest intensity was in agreement with our expectation, only parent ions could be observed, the intensity was not sufficient for a dissociation. There is a consistency between integrated peak values and ionization potentials (neglecting internal structure of the molecules): for N_2, the ionization potential is $I_p = 15.58$ eV, for O_2 12.07 eV and for H_2O 12.62 eV [42]. Thus, nitrogen should be harder to ionize than O_2 in a simple 'atomic picture' that does not account for molecular structure and in the limit of perturbative field strengths. We see a smaller signal, even if one takes into consideration that nitrogen is three times as concentrated in air. The reason why the water peak is so large compared to the oxygen with comparable ionization potential is because the pump rate for water is very small compared to the other air components[6].

---

[6] At a pressure of 10^{-3} torr, more than 75% of the remaining gas in the vacuum system is water vapor [43]

It should also be mentioned that a small peak at the trigger position is ringing from the Pockels cell of the amplifier, which is useful, as it makes it easy to estimate when the interaction took place and where in the oscilloscope trace. This little peak is present in all the data shown here.

At the middle intensity, the amount of N_2 that can be ionized increased by a large amount, while the O_2^+ peak stays almost the same, and the water peak became very small. We see the onset of dissociation because water gets dissociated and besides the H_2O^+ peak also H^+ can be observed. The O_2 is dissociated, too, and to a small extent maybe also nitrogen. The peak in figure 4.1 between the two grid lines for masses of 14 and 16 amu might therefore be a combination of signal from mainly O^+ and a little N^+. What is interesting is the fact that the hydrogen peak, as well as this oxygen peak, arrive too early, *i. e.* they get some kinetic energy from the electric field of the pulse or from acceleration when they get repelled by the other fragments. The effect of single hydrogen protons reaching the detector with a considerable additional kinetic energy has also been observed by Levis *et al.* [45] and others [48].

At the highest intensity, few intact parent ions can be observed. One sees large peaks of O^+ and N^+. The arrival time of the H^+, N^+ and O^+ peaks is not consistent with zero kinetic energy, and there are peaks that can only be explained by multiply charged species. This can also be concluded from their relative distances.

What can also be seen in figure 4.2 is that for increasing intensities the whole spectrum moved slightly to shorter flight times, *e. g.* the O_2^+ peak. We found out later that the 50 Ω terminator we used to ground the top plate

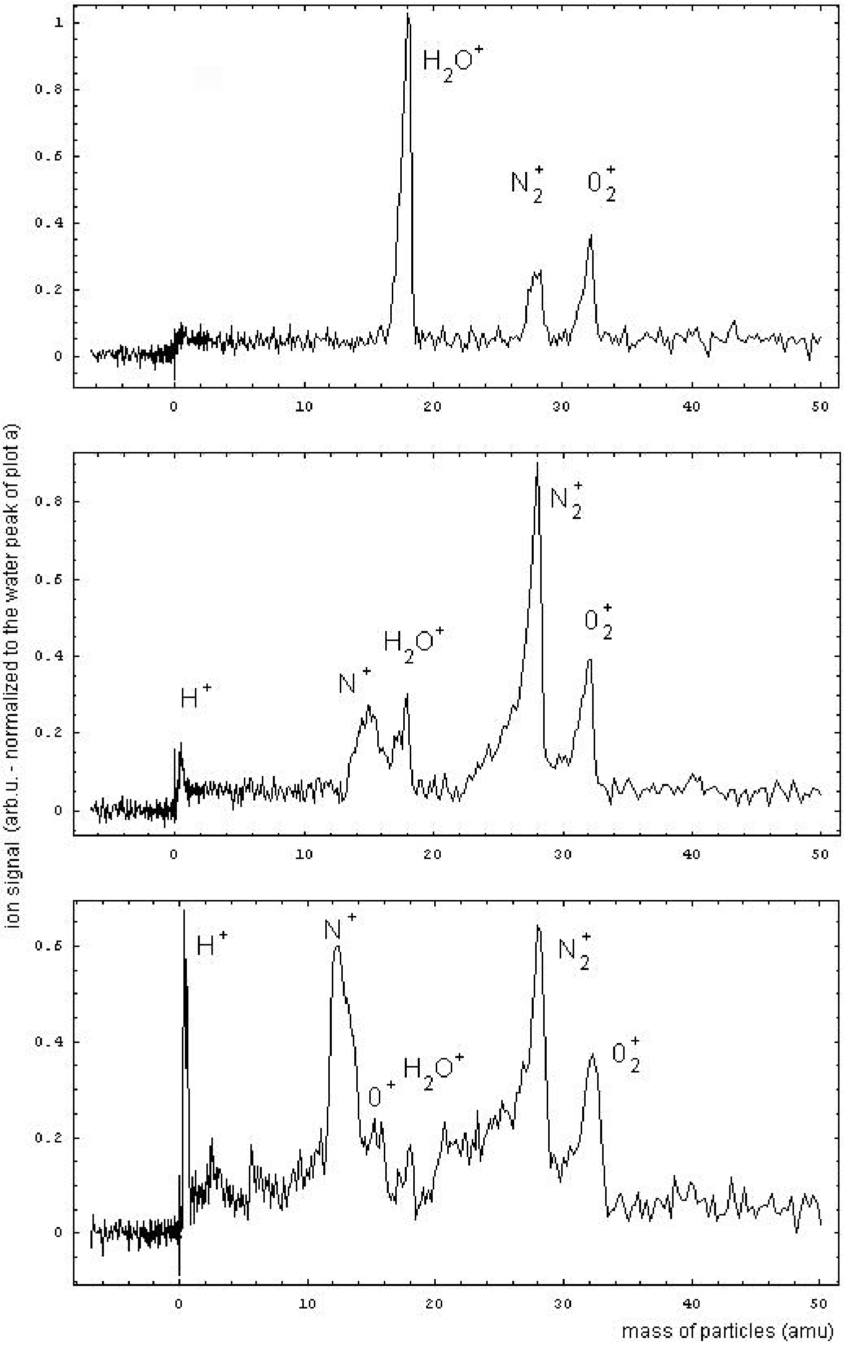

Figure 4.2: Mass–calibrated TOF traces for the ionization of air at intensities of a)$1.7 \cdot 10^{14}$ Wcm^{-2}, b)$3.8 \cdot 10^{14}$ Wcm^{-2} and c)$1.2 \cdot 10^{15}$ Wcm^{-2}

of the capacitor does not keep the top plate at ground, but allows for some charging of the plate which cannot completely discharge before the subsequent laser shot, so the top plate charges up. This is of course more evident at higher intensities where there are more charges created per shot of the laser. This explains a general shift of the peaks at higher intensities, because all ions are accelerated by the additional charge on the plate in the same way. This can also happen if the nozzle charges up. A confirmation that the shift is a charge effect was found by looking at the small peaks that were identified as O^{2+}, N^{2+} and 0^{3+}, N^{3+}. The ratio of the shifts in arrival times is $2 : 3$ (with a deviation of about 5%). If there is space charge or acceleration through other ions, lighter fragments should be more affected than heavier ones.

Figure 4.2 shows the same data rescaled with mass calibration. The calibration was done using time zero and the N_2^+ peak. The parent ion peak is very important for the calibration because the parent molecules are the only ones that have zero kinetic energy initially in the frame of the moving molecular beam.

4.2 Methanol Measurements

Methanol (CH_3OH) is the lightest alcohol with a molecular mass of 32 amu. Its ionization potential is 10.84 eV. The behavior of methanol in a very intense femtosecond laser field has most recently been examined by Wu *et al.* [51]. They made their experiments with an intensity of $2 \cdot 10^{15}$ Wcm^{-}2 and observed a Coulomb explosion. A Coulomb explosion is a process where several electrons are stripped off before the atoms in the molecule have a chance to change their center of mass position. The highly charged molecular ion then breaks apart due to the Coulomb repulsion. The interesting difference to fragmentation directly by the laser is the appearance of multiply charged cations with additional kinetic energy.

We performed this experiment after the air experiment at the same intensities of $1.7 \cdot 10^{14}$ Wcm^{-2}, $3.8 \cdot 10^{14}$ Wcm^{-2} and $1.2 \cdot 10^{15}$ Wcm^{-2} in the focus. The results can be seen in figure 4.3, where a is the lowest and c the highest intensity. Each plot is an average of 500 single traces with each trace representing the ion spectrum for a single laser shot. At the low intensity we see residual water at 18 amu (see figure 4.4) and a peak at 32 amu, which is a combination of O_2^+ and the parent ion. Comparing with the air measurement in figure 4.2, there are several differences. First, there is signal between 28 amu and 32 amu, which represents methanol molecules that have been deprotonated once or more times (hydrogen does not appear as an own ionic peak). Second, there is an oxygen peak at 16 amu that was not observed in air, therefore it must be from the oxygen in the methanol. Also, some OH^+ can be seen at 17 amu.

At the middle intensity, the parent ion peak is significantly reduced, while the peak at 28 amu dominates the spectrum, which is a mixture of N_2^+ and CO^+. Like in air, the N^+ peak appears and is shifted towards earlier arrival times. The most remarkable peak is the hydrogen peak that appears. It is very broad and looks more like two peaks where the one that arrives first is smaller. The same can be seen at our highest intensity. Although this is a

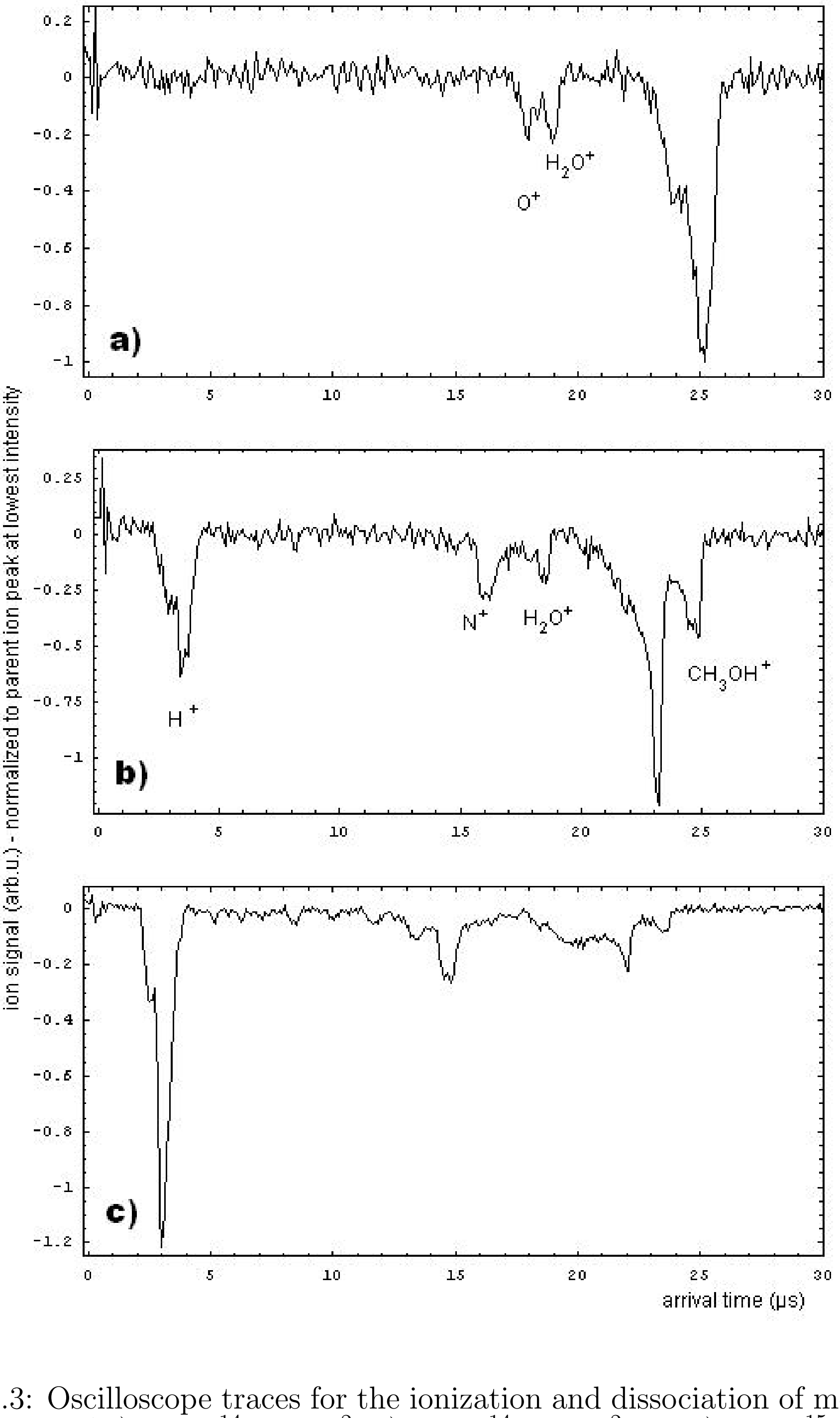

Figure 4.3: Oscilloscope traces for the ionization and dissociation of methanol at intensities of a)$1.7 \cdot 10^{14}$ Wcm^{-2}, b)$3.8 \cdot 10^{14}$ Wcm^{-2} and c)$1.2 \cdot 10^{15}$ Wcm^{-2}

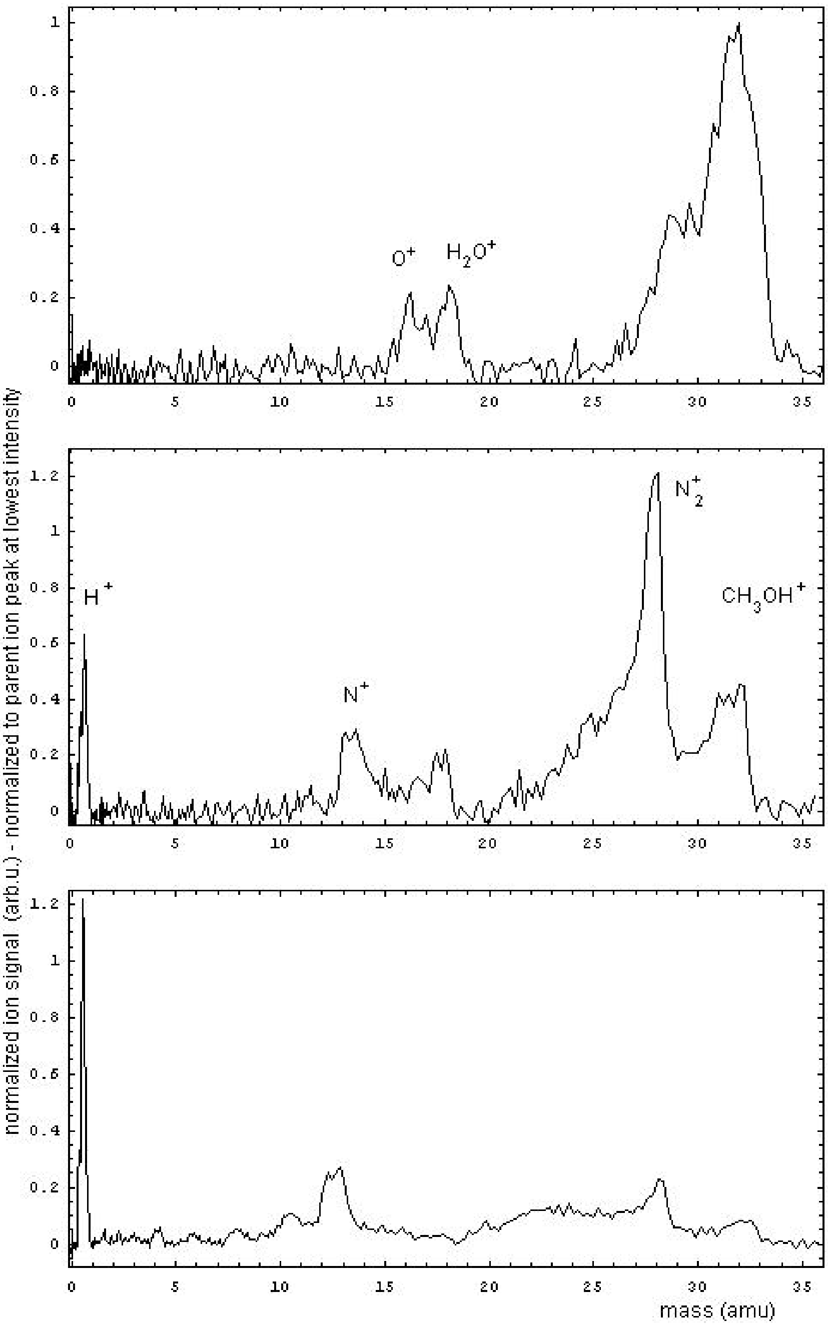

Figure 4.4: Mass–calibrated TOF traces for the ionization and dissociation of methanol at intensities of a)$1.7 \cdot 10^{14}$ Wcm^{-2}, b)$3.8 \cdot 10^{14}$ Wcm^{-2} and c)$1.2 \cdot 10^{15}$ Wcm^{-2}

small effect, it has also been observed by Wu *et al.* [51]. This peak gives rise to two conjectures: first we have a Coulomb explosion and the substructure in the hydrogen peak is caused by forward and backward kinetic energy distribution relative to the TOF tube (≈ -20 to 20 eV initial kinetic energy). If this is true, then second we might be able to conclude that we really had a problem with an upcharging top plate, because the second peak, composed of protons that approach the bottom plate first, is larger, which could mean that they do not see a charge effect of the same magnitude that the others do.

Evidence for the production of a Coulomb explosion can be seen in 4.3c, where we can clearly see small peaks at $\frac{m}{q}$ equal to 4, 6 and 8 and also a similiar structure at even smaller $\frac{m}{q}$. These peaks represent multiply charged carbon, nitrogen and oxygen cations. Compared to the air measurement, the integrated H^+ peak is immense, another indication that the methanol underwent a Coulomb explosion.

This experiment was in good agreement with Wu *et al.* [51]. Unfortunately we did not reach the resolution they had because of data acquisition problems that are currently being resolved.

4.3 Benzene Measurements

Benzene(C_6H_6) is the smallest aromatic molecule at a molecular weight of 78 amu. Its ionization potential is 9.24 eV, close to that of acetone (9.70 eV) and much smaller than that of the main air constituents. The ionization behavior of benzene and other molecules has been studied by Levis *et al.* in ref. [46, 47] at intensities up to $3.8 \cdot 10^{13}$ Wcm^{-2}. They mainly looked at the ionization rate of the parent molecule but did not study any dissociation, which requires higher intensities.

Some of our results can be seen in figure 4.5. The trace in 4.5a was taken at an intensity far below 10^{14} Wcm^{-2}. It agrees with previous results by Levis *et al.* [46, 47]: a very sharp and intense peak corresponding to the parent ion $C_6H_6^+$, but no fragmentation. The figures 4.5b and c where taken at intensities of $7.6 \cdot 10^{13}$ Wcm^{-2} and $2.1 \cdot 10^{14}$ Wcm^{-2}. Several different ion peaks can be observed. In figure 4.6 the x–axis has been scaled to molecular mass by using the trigger time and the parent ion peak arrival time for the transformation to mass calibration.

In figure 4.6 one can see the parent ion $C_6H_6^+$ on the right. For the higher intensities the parent ion peak broadens towards lower masses, because also $C_6H_n^+$ $(n < 6)$ are generated. Further to the left, there are very tiny peaks, one at around a mass of 58 amu (this is actually residual acetone from a previous experiment inside the chamber and the molecular beam setup). The following peak at around 50 amu is $C_4H_n^+$ $(n = 0 \ldots 4)$ because it is caused by fragments of benzene having four carbon atoms. The large and broad peak at around 38 amu originates from benzene dissociation into fragments with three carbon atoms $C_3H_n^+$ $(n = 0 \ldots 3)$. The only other peak that can be identified is at 18 amu and therefore is residual water in the beam [7].

---

[7] H_2O, O_2 and N_2 can also be seen in other TOF data: see ref. [45, 50] or especially water in ref. [51]

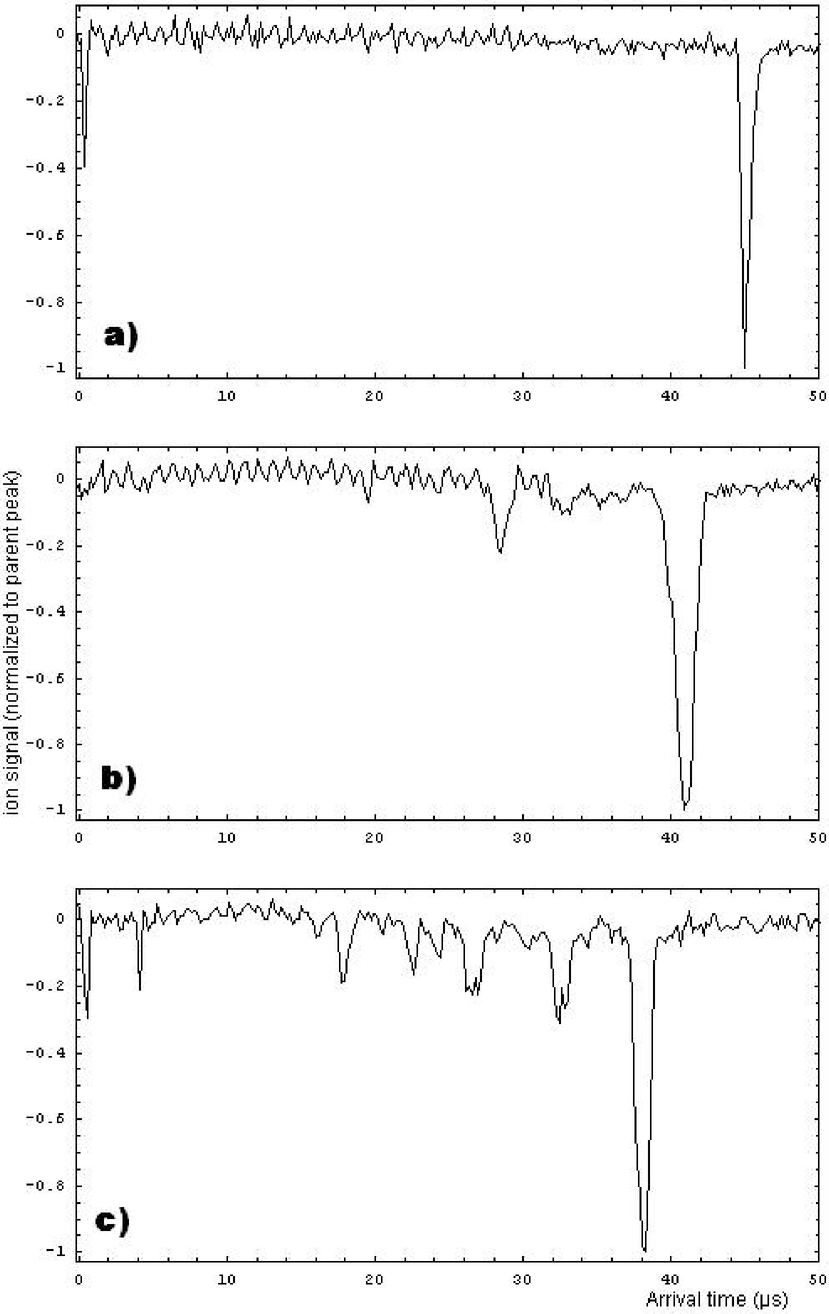

Figure 4.5: TOF spectra for benzene at intensities of a)≈ 10^{13} Wcm^{-2}, b)$7.6 \cdot 10^{13}$ Wcm^{-2} and c)$2.1 \cdot 10^{14}$ Wcm^{-2}

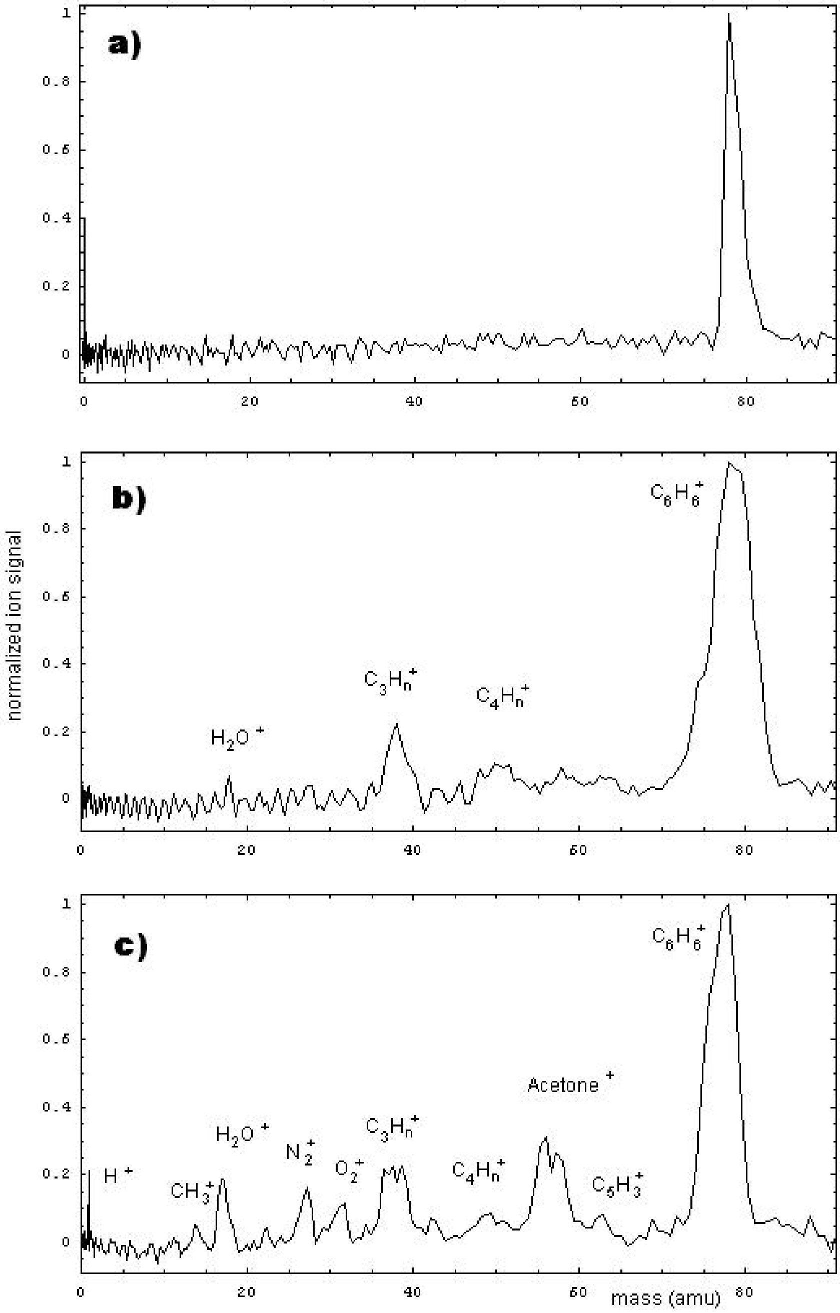

Figure 4.6: Mass–calibrated TOF spectra for benzene at intensities of a) $\approx 10^{13}$ Wcm^{-2}, b)$7.6 \cdot 10^{13}$ Wcm^{-2} and c)$2.1 \cdot 10^{14}$ Wcm^{-2}

The picture changes for the higher intensities, with several interesting new features appearing. The parent ion peak is more narrow than it was for the middle intensity, because the aromatic carbon ring is destroyed rather than deprotonated. Smaller peaks representing fragments such as $C_5H_3^+$ (63 amu) as well as N_2^+ and O_2^+ can be observed. The acetone peak increases significantly and splits up into parent and deprotonated ions. At 42 amu we see the acetyl ion CH_3CO^+, an acetone without a CH_3, whose ion shows up at 15 amu in the trace[8]. The two most interesting changes can be seen in the $C_3H_n^+$ and $C_4H_n^+$ peaks: the latter one seems to become smaller, while the first one increases its area. The peak structure suggests three peaks at 37, 38 and 39 amu, namely C_3H^+, $C_3H_2^+$ and $C_3H_3^+$, although we reached the limit of resolution with the number of traces for this data set. So the intensity might not only change the amount of dissociation, but also the branching ratio for the different dissociation channels. This coincides with the appearance of a H^+ peak that could not be observed at lower intensities.

These tests of the apparatus with benzene made us understand most of the features of the time–of–flight spectrum in both technical details and molecular physics. We see fragmentation that depends on the intensity of the laser pulse, multiply charged ions and protons with a significant initial kinetic energy.

Further experiments will be very interesting. Very recent dissociation

---

[8] At the high intensity all peaks drifted slightly to earlier arrival times, especially the smaller fragment peaks. We think this is mainly due to the "slow" 50 Ω resistance between ground and the capacitor top plates, which causes a charge–up of the plate

experiments with benzene that examined the translational energy given to H^+ fragments [48] and also pump probe ionization experiments [49] can be used as a starting point for new experiments with our setup.

Chapter 5

Acetone Measurements

Acetone (CH_3COCH_3) is the smallest ketone with a molecular mass of 58 amu. Its dissociation behavior for intensities in the region $0.7 - 1.1 \cdot 10^{14}$ Wcm^{-2} has recently been studied by Tang *et al.* [52]. We used acetone to test out the pump–probe apparatus and to see how circular polarization influences our signal.

5.1 High Intensities

The low intensity region has been studied and is in agreement with a stepwise process for the dissociation (see Tang *et al.* [52]). There are different dissociation thresholds for different bonds of the molecule. By increasing the intensity, it is possible to open new dissociation channels where a bond can be broken that was unbreakable at lower intensities. Therefore 'stepwise' refers to the appearance of new fragment ions once the intensity exceeds the dissociation threshold of the corresponding bond.

We made our first measurements of the dissociation of acetone with intensities of $1.7 \cdot 10^{14}$ Wcm^{-2}, $3.8 \cdot 10^{14}$ Wcm^{-2} and $1.2 \cdot 10^{15}$ Wcm^{-2} (see figure 5.1). These intensities were too high to see the stepwise dissociation of acetone. At the lowest intensity we observed a strong parent ion peak, the acetyl ion CH_3CO^+, and the presence of smaller peaks of CH_3^+, CH_3C^+ and 0_2^+. For short arrival times there is already a considerable H^+ peak. Multiply charged species provide evidence for a Coulomb explosion, which is already indicated at this intensity by small peaks. For the higher intensities these multiply charged ion peaks become larger and new ones appear. At the highest intensity the C^{3+} peak dominates, but already at lower intensities fragments with $\frac{m}{q}$ smaller than 12 $\frac{amu}{e}$ were detected.

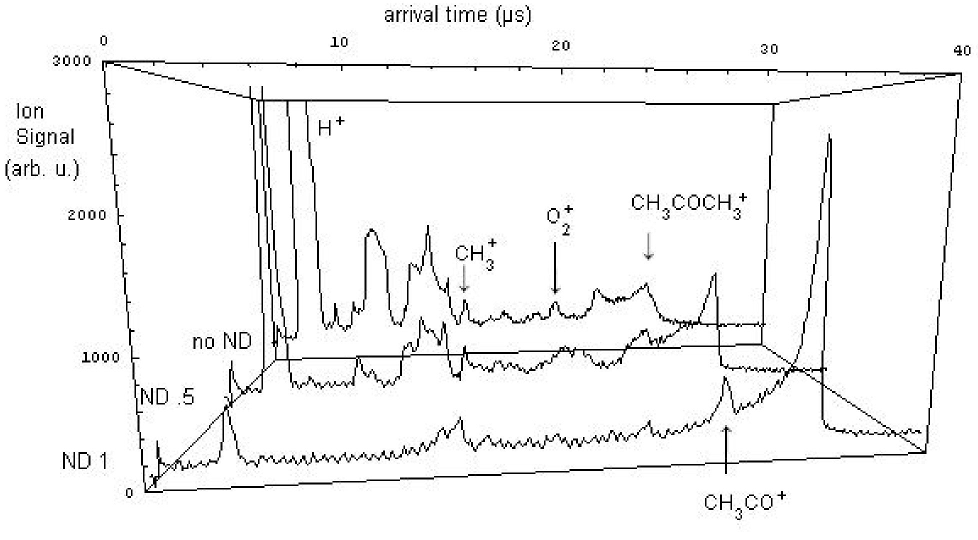

Figure 5.1: Oscilloscope traces for the ionization of acetone at intensities of a)$1.7 \cdot 10^{14}$ Wcm^{-2}, b)$3.8 \cdot 10^{14}$ Wcm^{-2} and c)$1.2 \cdot 10^{15}$ Wcm^{-2}

This Coulomb explosion was actually not what we intended to see and so these measurements are only of minor relevance for the research we plan to carry out with the apparatus. Nevertheless, they are very interesting because they demonstrate that the pulses from our amplifier can easily dissociate many different molecules, that we are able to understand the TOF spectra, that there is rich underlying dynamics with many different regimes. Furthermore, they give us an idea of processes that can occur to other molecules with high intensities.

The asymmetry of the parent ion peak, best seen at the lowest intensity, differed from our expectation of the spectrum. As the parent ion peak cannot get additional kinetic energy from the laser pulse, the asymmetry is not due to the ionization process itself. It is possible to take one or more hydrogen atoms away from the molecule, what would result in an ion signal corresponding to masses of $51 - 58$ amu, but the asymmetry can be seen in the whole region between the parent ion peak and the CH_3CO^+ peak that corresponds to a mass of 43 amu. Thus, we conclude that this is not the reason for the asymmetry either.

The asymmetric behavior was not observed when we used another lens (an achromat) that compensated for spherical aberrations. Therefore, we think that the distribution of space charge was different for the lens used in the measurement of figure 5.1, because the focal volume was larger than for the achromatic lens, so that the observed asymmetry is a consequence of space charge.

5.2 Pump Probe Data

In our Mach–Zehnder interferometer the deformable mirror pulse shaper allows for changing the duration and the shape of the pulse. The data in figure 5.3 has been recorded with a probe of 40 fs and probe beams of 114 fs and 189 fs. The intensity at time zero (*i. e.* the combined intensity of both pulses) in the focus was $2.0 \cdot 10^{14}$ Wcm^{-2} for the 114 fs and $1.7 \cdot 10^{14}$ Wcm^{-2} for the 189 fs pump pulse. The probe pulse contributed an intensity of $1.4 \cdot 10^{14}$ Wcm^{-2}, while the pump pulses had an intensity of $5.8 \cdot 10^{13}$ Wcm^{-2} (114 fs) and $3.5 \cdot 10^{13}$ Wcm^{-2} (189 fs) in the focus. Reconstructed intensity and phase based on FROG data of the three pulses can be seen in figure 5.2. For those parts of the pulses where the intensity is not clearly above the noise level, the phase are irrelevant.

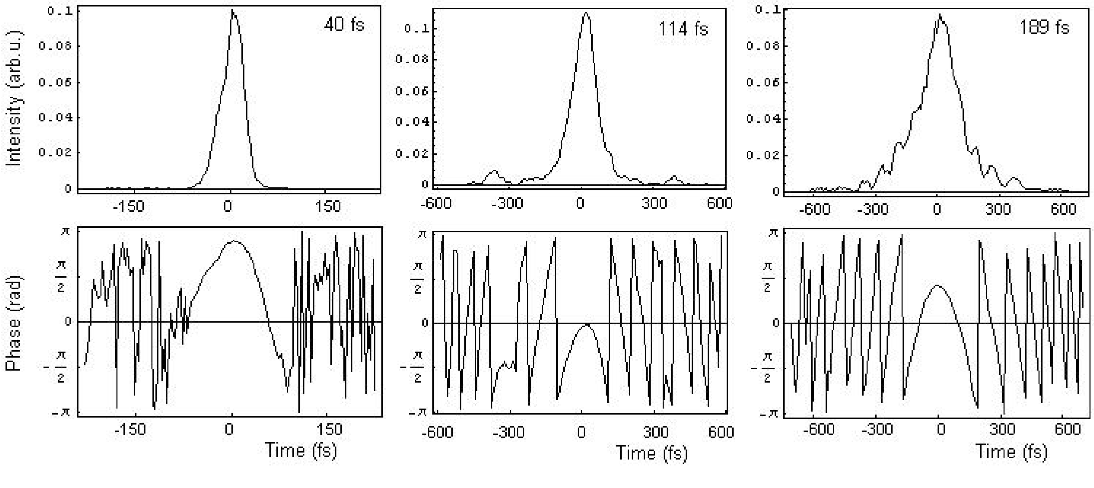

Figure 5.2: Reconstructed intensity and phase for the 40 fs probe and the 114 fs and 189 fs pump pulses

The different pump beams totally change the behavior of the ion spectrum as a function of pump probe delay. In the case of the shorter pump pulse (top) the parent ion signal gets smaller at time zero. When the pulses begin to overlap, one would expect an increase in the parent ion signal, which is not observed. This might be due to saturation, *i. e.* the maximum amount of molecules is already ionized by the two non–overlapping pulses. When the overlap becomes stronger, the intensity of the light in the focus is the combination of both pulses, as they sum up. As can be seen from the TOF spectra shown earlier, fragmentation increases with increasing intensity, so the share of dissociation is rising.

With the longer pulse the $CH_3COCH_3^+$ peak is increasing at time zero. The saturation might therefore not yet be achieved. That means the probe and this shorter pump pulse cannot ionize everything, in contrast to the pump probe scan with the short pump pulse.

It is also possible that the chirp of the pump pulse plays an important role in changing the behavior of the parent ion peak near time–zero. This point requires further investigation in future experiments.

Taking a closer look onto the top picture in figure 5.3 one can also the appearance of H^+ signal during the time the two beams overlap temporally, as well as a pale line of CH_3C^+ between the water and the CH_3CO^+ line. Furthermore, the parent ion pulse is smeared out at time zero. We believe that this is due to the creation of $CH_3COCH_n^+$ $(n < 3)$. This is another indication that dissociation is increased at time zero. The shift that all the peaks undergo is discussed in the following section.

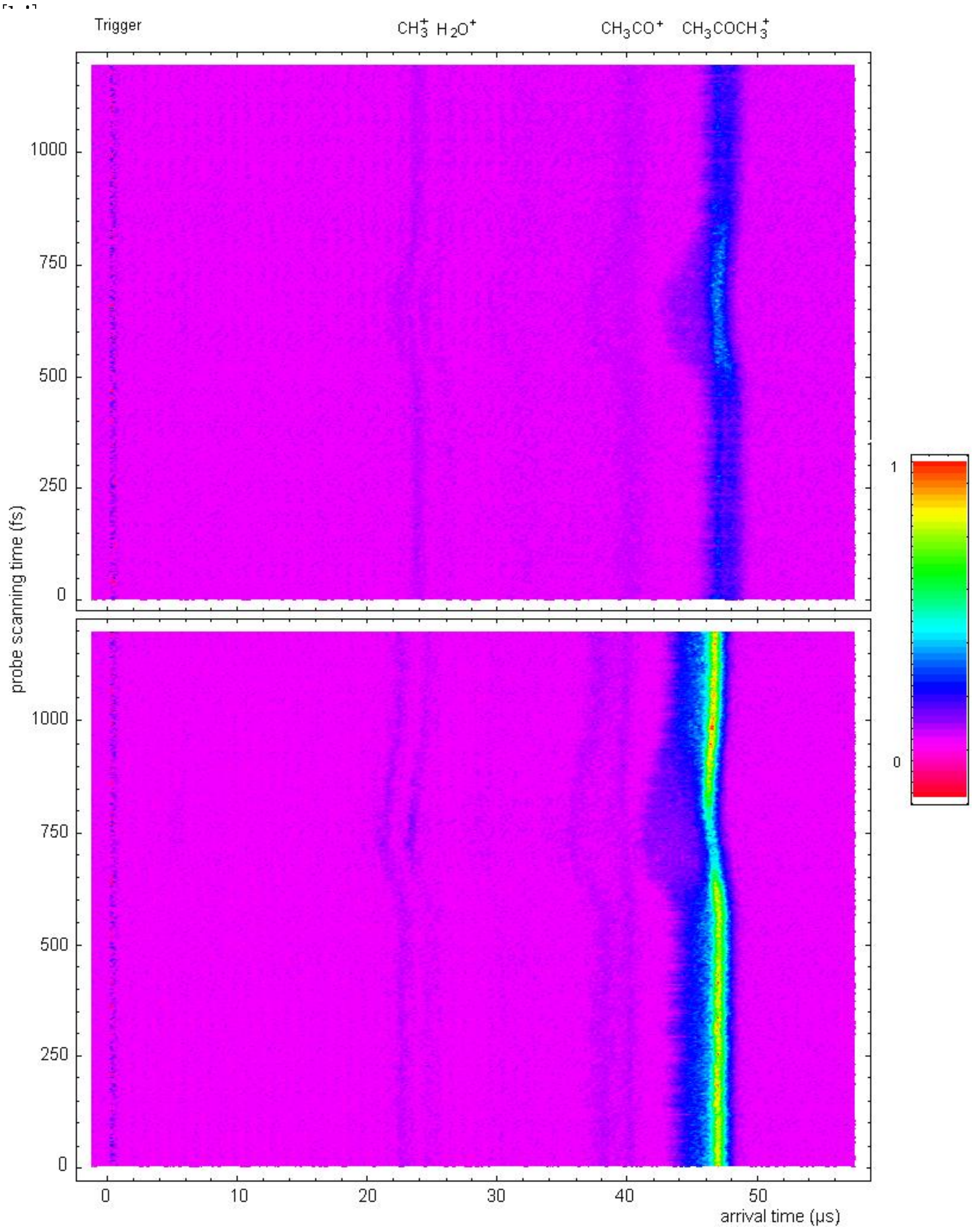

Figure 5.3: Pump probe experiment with a 40 fs duration probe pulse and pump pulses of 114 fs (bottom) and 189 fs (top) duration

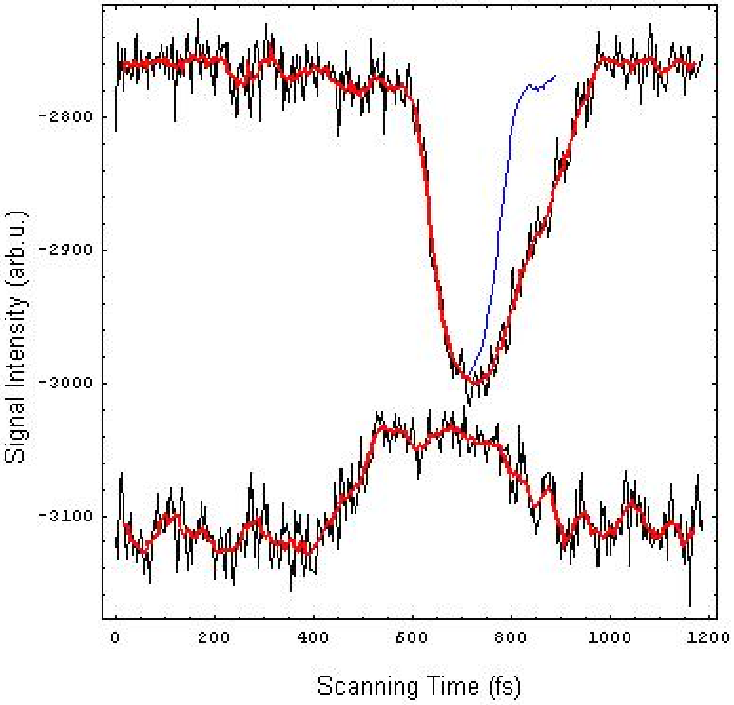

Figure 5.4: Boxcar–integrated parent ion signal for 114 fs (top) and 189 fs (bottom) pump beams; smoothed curves are shown red; the blue curve represents a mirror of the positive slope

To gain more information about the region near time–zero, we made a boxcar–integration around the parent ion signal, as shown in figure 5.4. Of course, the average signal for the longer pump pulse (bottom, increasing signal at time zero) is lower than for the shorter one (top, decreasing signal at time zero). In both cases the slope is steeper when the pump catches up with the tail of the probe. The two integrated ion traces have a duration of (215 ± 10) fs and (360 ± 15) fs, which is longer than expected from an autocorrelation of the two pulses based on the electric field as measured by the FROG, by time spans of 100 fs and 170 fs. The blue line in the upper graph is an image of the earlier points at the time where the slope of the signal is becoming level. If the ion peak were symmetric in time with an equal rise and fall time, then it would have a duration of 120 fs. One can conclude that the asymmetry is caused by a molecular effect that might be explained by an intermediate state that is easier accessed by the probe and ionized by the pump than vice versa. This is also what can be seen in the asymmetric shifts of figures 5.7 and 5.3. The state would have a lifetime of a few hundreds of femtoseconds. Furthermore, the smoothed signal (red curve) shows an interesting substructure with a repetition rate of about 100 fs. This could be another indication for intramolecular dynamics.

5.3 Polarization Effects

Several experiments have been undertaken to study the influence of the polarization of the incoming light on the dissociation process. Couris *et al.* [53] have shown that there is a relation between linear polarization and the angular distribution of the ions when generated by using pulses of $200 - 500$ fs. This is due to laser–induced alignment before the actual dissociation occurs.

However, when shorter pulse durations are used, there is no time for alignment. We are interested in processes that lead to dissociation of the molecules. The parent ion will generally be the easiest ion to produce, while higher intensities are needed for dissociation. Circular polarization can influence the ionization process of the molecule, like it has been recently done by Wu *et al.*

for methanol [51] or by Müller *et al.* for toluene [54]. Another interesting experiment has observed the differences of left and right circularly polarized light on chiral molecules [55]. There have been little studies on the influence of circularly polarized light on the dissociation process of molecules. It might be possible that dissociation and ionization are influenced in different ways, so that *e. g.* the parent ion signal can be reduced while dissociation channels are less affected. Therefore, circular polarization studies are of special interest for our experiments that concentrate on dissociation, because it may be a useful tool in keeping ionization from the pump pulse to a minimum.

The ionization of molecules with near–infrared light pulses is a multiphoton process (*e. g.* seven photons from a wavelength of 800 nm are necessary to ionize acetone). The ionization signal is greatly enhanced by intermediate resonances, where an intermediate state is reached by one or more photons and the ionization is completed from this state.

In an example where there is a three photon process with a two photon resonance, there are two ways to ionize the molecule. If we write the initial state as $|1\rangle$, the two photon intermediate resonant state as $|2\rangle$, and the continuum state as $|k\rangle$, then if three photons are absorbed nonresonantly, the coupling between $|1\rangle$ and $|k\rangle$ can be described by a third order matrix element

$$V_{1k}^{(3)} = \sum_{j_1} \sum_{j_2} \frac{\langle 1|\frac{\mathbf{ED}}{2}|j_1\rangle\langle j_1|\frac{\mathbf{ED}}{2}|j_2\rangle\langle j_2|\frac{\mathbf{ED}}{2}|k\rangle}{(\omega_1 + \omega - \omega_{j_1})(\omega_1 + 2\omega - \omega_{j_2})} \tag{5.1}$$

$$|j_1\rangle, |j_2\rangle \neq |1\rangle, |2\rangle, |k\rangle$$

while the coupling via the resonance can be described by a second–order and a first–order element [59]:

$$V_{1k} = V_{12}^{(2)} \cdot V_{2k}^{(1)} = \left[\sum_j \frac{\langle 1|\frac{\mathbf{ED}}{2}|j\rangle\langle j|\frac{\mathbf{ED}}{2}|2\rangle}{\omega_1 + \omega - \omega_j} \right] \cdot \langle 2|\frac{\mathbf{ED}}{2}|k\rangle \tag{5.2}$$

$$|j\rangle \neq |1\rangle, |2\rangle, |k\rangle$$

where E is the field strength and D the dipole operator. Non–diagonal elements of order 2 or higher are neglected. One can see that the matrix element describing the three photon process is much smaller. Thus, the contribution from the resonance dominates the process.

Any intermediate resonance en route to the continuum will greatly enhance the ionization signal. While in the weak field limit there is little chance of an intermediate resonance, in the strong field of a femtosecond laser pulse, intermediate states can Stark shift into resonance. Thus, the strong field ionization signal from atoms in femtosecond laser fields is largely due to paths to the continuum which involve intermediate resonances.

In atomic ionization, if the atom is in the ground state ($l = 0$), and *e. g.* can be excited to an intermediate state with $l = 1$ using three photons, the ionization signal is increased due to resonance–enhanced multiphoton ionization. On the contrary, if the light comes in circularly polarized, the $l = 1$ state cannot be reached by a three photon process because the angular momenta of the photons have to add up to 3. Therefore, with circular polarization, resonant ionization enhancement can be turned off, like is has been observed by Hertlein [56].

While molecular states are clearly different from their atomic counterparts, we expect some discrimination in the ionization signal for circular versus linear polarization as a result of intermediate resonances becoming inaccessible. The intramolecular processes that lead to dissociation instead of ionization of the parent ion might have a different dependence on the polarization of the light. Ideally, it would be nice to be able to switch off ionization while maintaining fragmentation for the pump. In a pump probe experiment, the circularly polarized pump could dissociate the molecule neutrally, followed by a probe that performs the ionization necessary for the detection of fragments in a TOF spectrometer.

We measured the dependence of the ionization signal on ellipticity by measuring the ion signal versus angle for a quarter waveplate inserted into the pump beam. The probe was not used in this experiment. The scale on the waveplate was turned from 0° to 45° in steps of 5° and 100 traces were averaged for each waveplate position. The energy per pulse was 84 μJ . A box car was put around the parent ion and the background–substracted integrated ion signal is plotted in figure 5.5. Müller *et al.* [54] observe a dependence on the ellipticity of the form

$$I(\theta) = I_{circ} + (I_{lin} - I_{circ}) \cdot \cos^2(2[\theta - \theta_0]) \tag{5.3}$$

This formula assumes that there is a linear dependence between the fraction of linearly polarized light and ion signal, which Müller *et al.* actually observed for toluene. Fitting our data to this model one can see that we observe more systematic deviations from the formula than Müller. These deviations seem

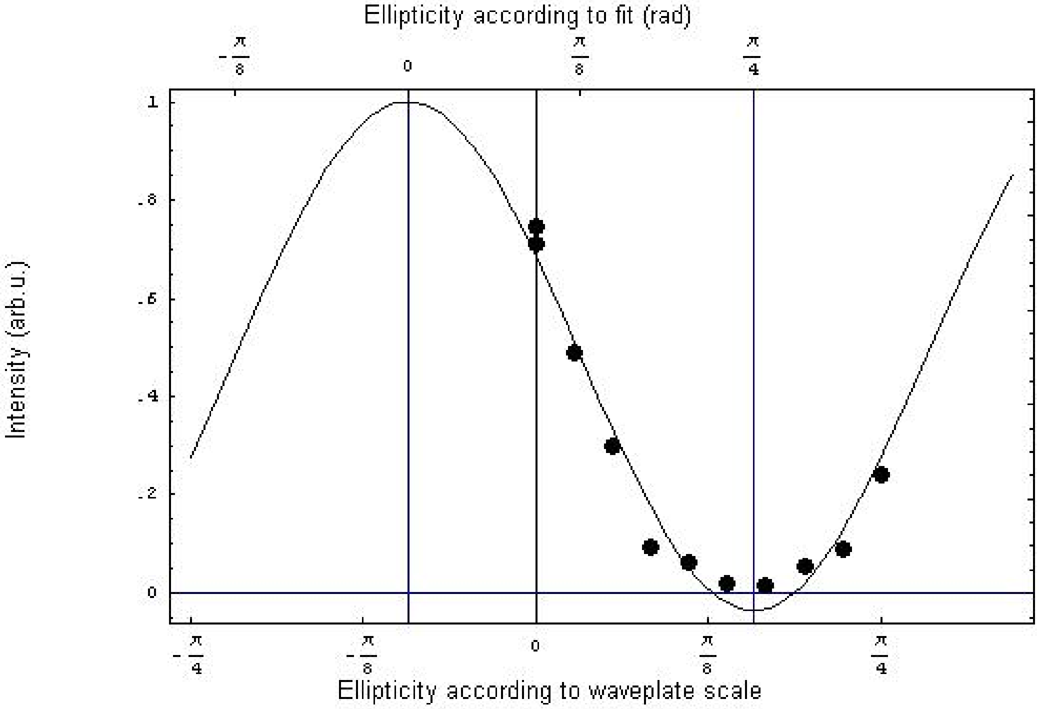

Figure 5.5: Total parent ion signal of acetone as a function of the ellipticity of the laser beam

to be systematic at lowest signal rates. Also, the fit gives a value for I_{circ} of $(-35 \pm 23) \cdot 10^{-3})$ (I_{lin} normalized to one), indicating that our data set does not behave according to formula (5.3). This might give us information about the location of an intermediate resonance in acetone. Also, the fact that the parent ion signal actually can be reduced to almost zero intensity by turning the waveplate is useful for pump probe experiments.

The fit of the data to formula (5.3) results in an angular offset of $\theta_0 = 16.6° \pm 0.7°$. Assuming the labels on the waveplate are correct, this means our polarization is turned by 16.6° from the initial polarization, probably by the pulse shaper, or the polarization was not purely linear to begin with.

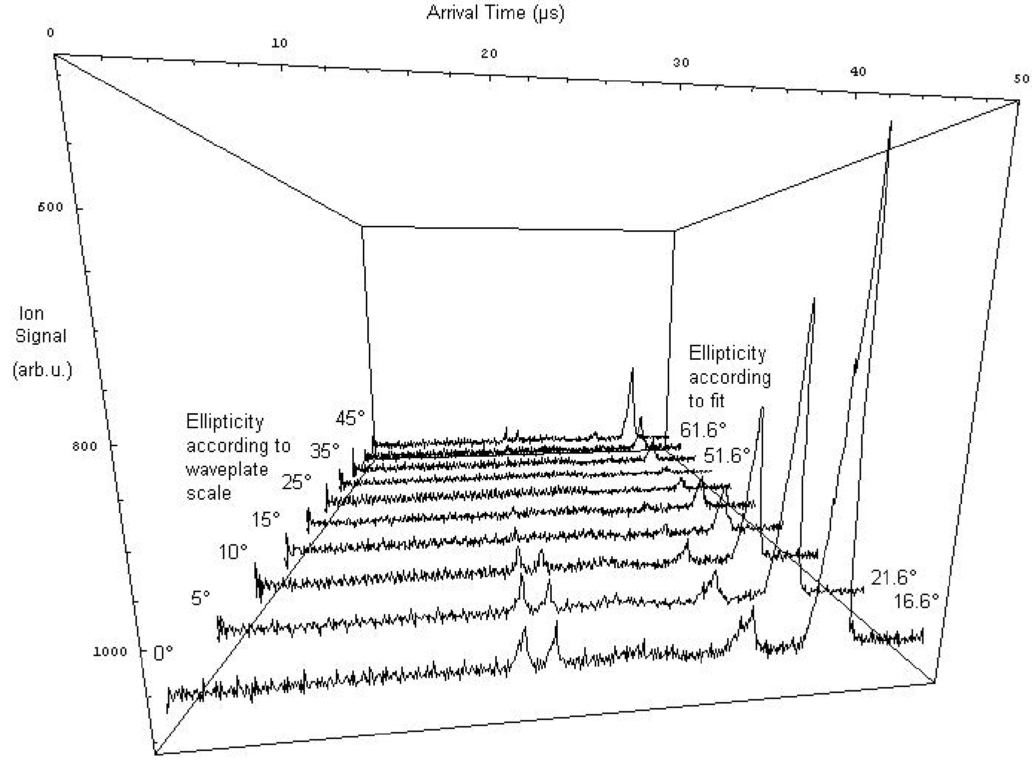

Figure 5.6: TOF spectra for acetone at different ellipticities of the laser beam

This experiment should be repeated soon to record more data points for different angles and to see whether the deviation from (5.3) is reproducible. In figure 5.6 the traces for different ellipticities of the light are plotted. From right to left the peaks are the parent ion $CH_3COCH_3^+$, the acetyl ion CH_3CO^+ and CH_2CO^+, residual water H_2O^+ and CH_3^+. The ellipticity might have different impacts on the two channels leading to parent ionization and dissociative ionization, although our resolution has not been good enough to observe this yet. This would be another example of how circular polarization can help to separate dissociation from ionization.

Getting one step closer to the final goal of pump probe learning control, we made a pump probe experiment with a circularly polarized pump beam. We used a 40 fs probe pulse and a pump pulse that was stretched by the deformable mirror setup to 120 fs and then circularly polarized by the quarter waveplate. The contour graphs in figure 5.7 show ion signal versus arrival time and probe scanning time. The pulses temporally overlap at a scanning time of $\approx$ 605 fs. For scanning times larger than 605 fs the pump pulse is ahead of the probe pulse.

The top picture in figure 5.7 shows the scan with the quarter waveplate at 45° in the pump beam. As long as the pump is ahead and the beams do not temporally overlap, the signal of the parent ion stays most intense and relatively constant within the noise level. When approaching time zero, the intensity of the parent ion is dropping, like has already been observed in figure 5.3 for the case of both pump and probe polarization being linear. When the pump beam is ahead of the probe, the signal intensity of the parent ion does not reach the same level that it had before. First considerations that the laser intensity has dropped by chance can be abandoned because the CH_3^+ signal is not dropping but on the contrary, rising slightly.

In the lower plot of figure 5.7 we see the same experiment with the waveplate at 0°. It is obvious that the intensity on both sides of time zero is mainly

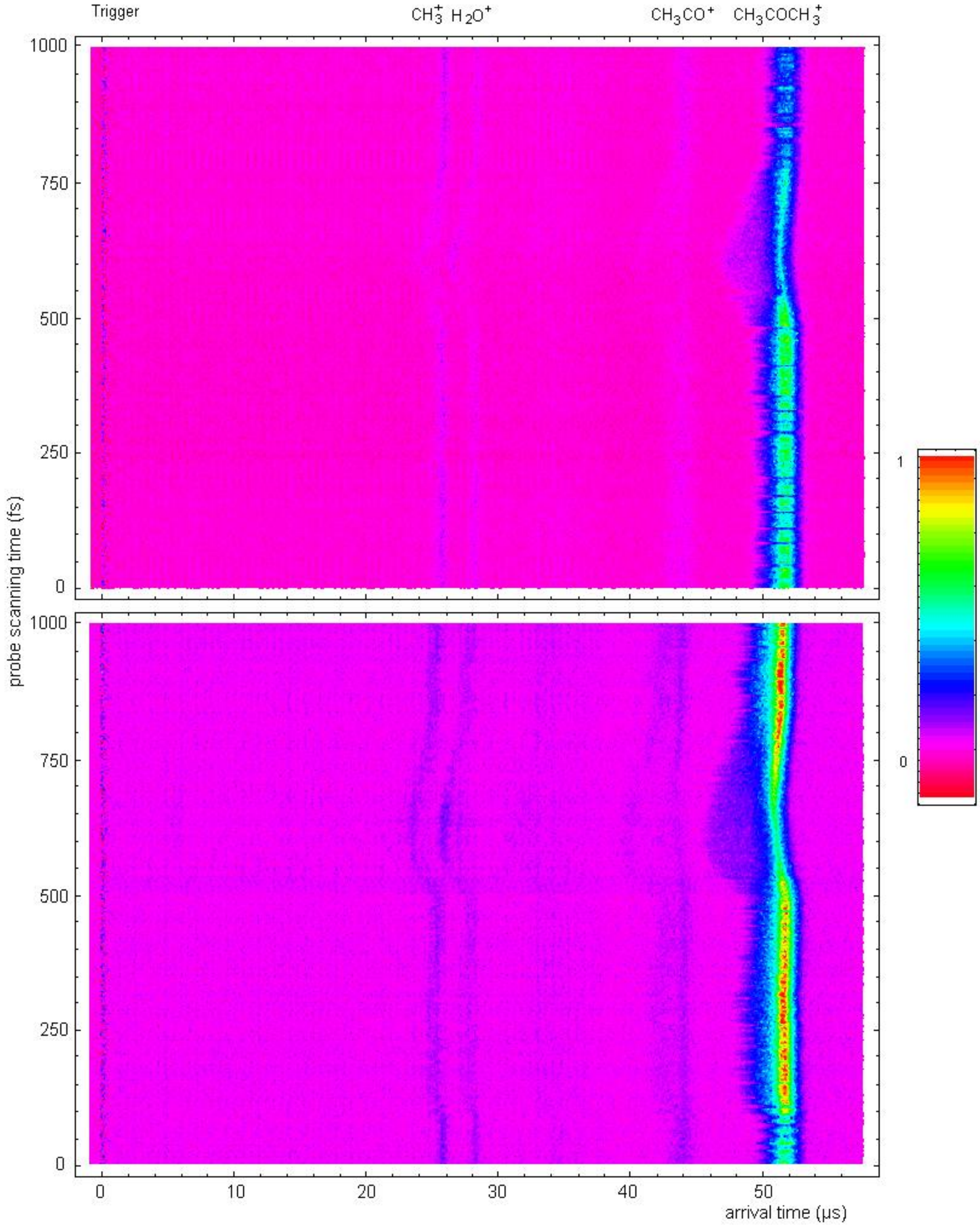

Figure 5.7: Waveplate pump probe experiment: with quarter–waveplate at 45° (top) and at 0° (bottom)

the same. An interesting point is the drop of intensity if the probe is too far ahead. Again, the idea that this is a drop in the laser intensity is refuted by an increase in the CH_3^+ signal by almost a factor of two, and also a slight increase in H_2O^+. It is not clear to us where that comes from. Another feature of the plot is an increase of H_2O^+ at around time zero, as one would expect because the intensity at the focus is larger and therefore ionization of water is easier to achieve.

For the experiments that we intend to pursue, the asymmetry of the parent ion peak about time–zero is of most interest. It shows that the pump pulse can dissociate the molecule while the probe performs the ionization afterwards. This general scheme is related to the internal structure of the molecule. We are trying to understand these observations in terms of specific molecular states for acetone. The first absorption band in acetone is the $\pi^* \leftarrow n$ $(S_1 \leftarrow S_0)$ transition [57]. The n is representing a non–bonding electronic orbital of the oxygen atom and π^* the excited state. The other notation stands for singlet states, with the ground state S_0 and the first excited state S_1. The second absorption band is the $3s \leftarrow n$ $(S_2 \leftarrow S_0)$ transition. Both can couple to an anti–bonding triplet state, which leads to spontaneous dissociation. There are also other resonances that can act as intermediate states for a following ionization of the parent molecule [57, 58].

The presence of circularly polarized light will change the selection rules for electronic transitions. It is possible that one or more resonances cannot be accessed by circularly polarized light. If the probe is first, this resonance can be excited and then further ionization can be done by the probe itself or the pump that comes later. In the case where the pump comes first, the intermediate state might not be accessed, so the signal for the parent ion is lower. It might also be possible that an anti–bonding state is populated more numerous instead, what would lead to neutral dissociation. The fragments can be ionized by the probe pulse. This assumption would be backed by an increase in CH_3^+ ions.

What can be seen in all of the plots is a drift of the peaks at time zero towards earlier arrival times, but not all of the peaks shift! The CH_3CO^+ signal splits into two parts, one of them is moving like the others, the other one is not affected. This drift could be due to charge effects, as the laser intensity and with this also the overall ionization rate is largest. The peak that is not moving apparently does not see this charge effect, so the ion is presumably created after the others have left the capacitor. This could mean that there exists an excited $CH_3COCH_3^+$ state that decays into a CH_3CO^+ ion after a certain time, like Owrutsky *et al.* suggest in their work [58].

While in the experiment with the waveplate at 45° the shift of the ions is symmetric around time zero, it is not for 0°, where the slope of the shift looks steeper when the pump is right after the pulse than vice versa. This was also observed in the chirp experiment discussed in the previous section.

All the data discussed above gives rise to new ideas about undertaking acetone experiments.

5.4 Correlation Coefficient

Another very helpful tool to understand our three–dimensional data is a correlation map. It includes information about which peaks are correlated. Furthermore, it helps to clarify whether there really is signal in regions where signal to noise is very small, and it shows internal structure of the signal that is not seen from the pure data. We made a correlation for the ion signal as a function of arrival time. To do so, we summed up the signal $I(p, z)$ for a certain oscilloscope pixel p over all stepper motor positions z for the delay between the two pulses. The correlation coefficient ρ is described by the formula:

$$\rho_{pp'} = \frac{\left[\frac{1}{N}\sum_{z=1}^{N} I(p,z)\cdot I(p',z)\right] - \left[\frac{1}{N}\sum_{z=1}^{N} I(p,z)\right]\cdot\left[\frac{1}{N}\sum_{z=1}^{N} I(p',z)\right]}{\sigma_p \cdot \sigma_{p'}} \tag{5.4}$$

where the standard deviation σ_p is given by

$$\sigma_p = \sqrt{\left[\frac{1}{N}\sum_{z=1}^{N} I(p,z)^2\right] - \left[\frac{1}{N}\sum_{z=1}^{N} I(p,z)\right]^2} \tag{5.5}$$

Two signals are perfectly correlated when the correlation coefficient is equal to 1, and perfectly anticorrelated if it is equal to -1. The correlation coefficient for the ion signal at different arrival times of the lower plot in figure 5.3 is shown in figure 5.8. Of course, the picture has to be symmetric around the diagonal, on which the correlation coefficient is equal to 1.

It is not clear where the regular stripes come from that only appear where there is zero signal. It might be an artifact of the oscilloscope (the frequency of that disturbance is 1 MHz) or the Mathematica software I used.

Several interesting things can be seen. The Pockels cell ringing when our light pulse enters the chamber (at arrival time 0 μs) is not correlated

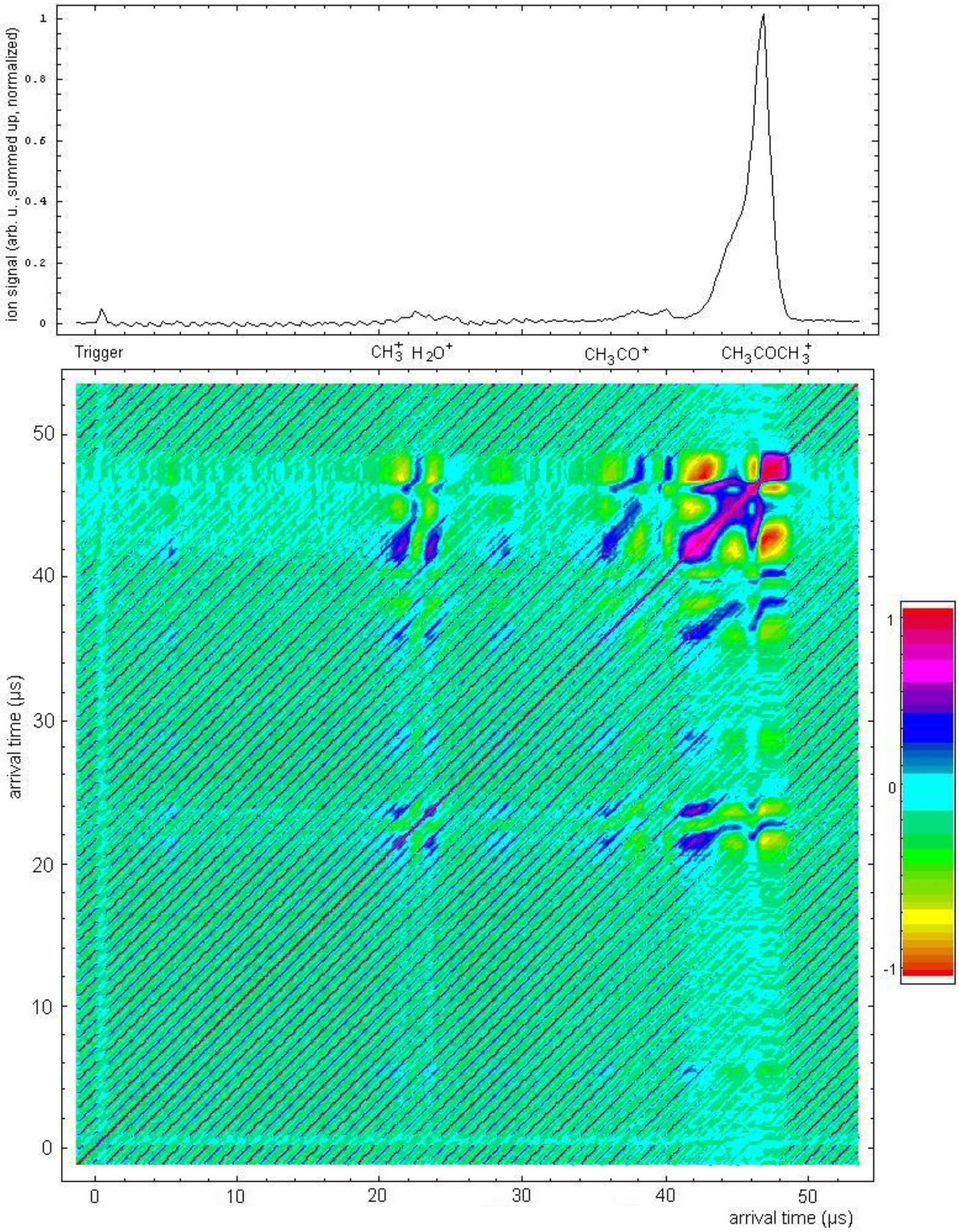

Figure 5.8: Top: Integrated ion signal for different arrival times (oscilloscope pixels); Bottom: Correlation coefficients for different arrival times (oscilloscope pixels)

to any other peak. The first deviation from zero can be seen at an arrival time of$\approx 5\mu$s, where there is a signal that is anticorrelated to the parent ion signal, but correlated to the region where $CH_3COCH_n^+$ $(n < 3)$ is found. This deviation corresponds to H^+ ions that appear more numerous where the parent ion signal is decreased. The same behavior can be seen for the following CH_3^+ and H_2O^+ peaks. Looking at an arrival time of 28 μs, one can see that there is another signal that was hard to see in the pure data. From a calculation back to the mass that corresponds to this arrival time and observations by Tang *et al.* [52] we conclude that it is CH_3C^+.

As mentioned in section 5.3 the CH_3CO^+ peak is split into two peaks at high intensities, one that is shifting at time–zero like the CH_3^+ and water peaks and one that behaves like the parent ion peak. The correlation coefficient in figure 5.8 confirms this for the most part. The shifting peak centered around 28 μs is anticorrelated to the parent ion, but correlated to the $CH_3COCH_n^+$ as well as the CH_3^+ and the water. The non–shifting peak behaves the opposite way. This agrees with the interpretation given in the previous section.

The parent ion peak is almost perfectly anticorrelated to the $CH_3COCH_n^+$ $(n < 3)$ region at around 44 μs, where the correlation coefficient reaches its minimum of -0.83. Around the diagonal at the parent ion signal, we have values of close to 1. Right before this region, the small area of anticorrelation is due to the fact that the parent ion is drifting slightly towards earlier arrival times when the two laser pulses overlap temporally. The intensity for these earlier times increases at the expense of later times, thus this anticorrelation.

In addition to the correlation of different peaks figure 5.8 includes much more structure, especially in the region of the parent ion. It will be interesting to verify these dependencies in future experiments.

Another data analysis tool is the calculation of the center–of–gravity for the peaks. The center–of–gravity for each stepper motor position was calculated in a window p_{min} to p_{max}:

$$I(z) = \left[\sum_{p_{min}}^{p_{max}} I(p,z) \cdot p\right] / \left[\sum_{p_{min}}^{p_{max}} I(p,z)\right] \tag{5.6}$$

The result is the mean arrival time of the pulse as a function of time delay, as can be seen in figure 5.9. The center–of–gravity calculations are shown for the parent ion signal, and the CH_3CO^+ signal that splits into a slightly–moving and a strongly–moving peak. Several features in figure 5.9 are noteworthy. First, the fact that the peaks do not all move by the same amount indicates that not only charge effects are responsible for the shift. Second, the parent ion signal after passing time–zero is not going back to its initial arrival time, while it mostly does for the other two peaks. Thus, we conclude that this is another indication for increased dissociation if the pump pulse is ahead of the probe pulse. The remaining shift in arrival time is due to more signal from deprotonated parent ions that are taken into account in the center–of–gravity calculation. Third, the double peak structure in figure 5.9c is remarkable.

Considering that all three data sets have been taken in one measurement, this cannot be caused by an instability of the system or a miscalibration of the stepper motor. The reason for this double peak might again be an intramolecular effect. Thus, one could use the pulse shaper and the genetic algorithm

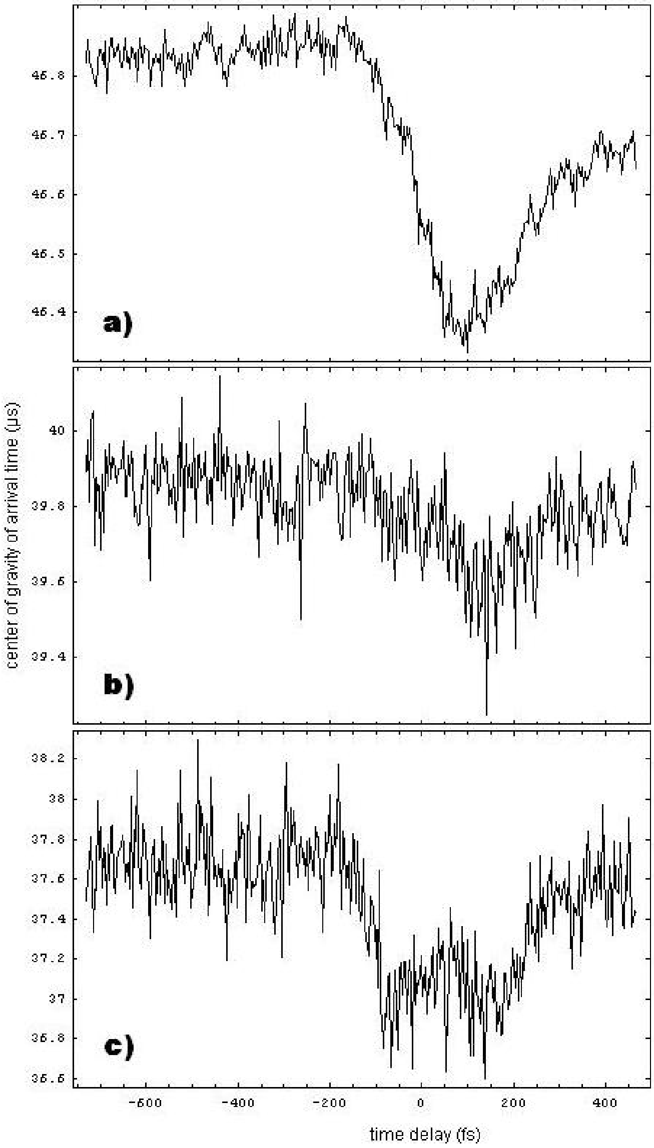

Figure 5.9: Center–of–gravity calculations for a) the parent ion signal; the CH_3CO^+ signal that b) only moves slightly, and c)moves stronger

to enhance one of the observed features. This could give rise to promising learning control experiments.

Chapter 6

Conclusions

In this thesis I have described the design and construction of an apparatus that can be used to ionize and dissociate molecules with ultrafast lasers. It is suitable for ionization, dissociative ionization and neutral dissociation experiments as well as for learning control in combination with the deformable mirror setup. Although several optimizations will be required constantly, it can be used right away for these purposes. The thesis can serve as an aid and overview of the setup for future students.

Some of the results acquired in testing the apparatus showed features in the dissociation of molecules that could be prosperous for prospective experiments, especially with the pulse shaper. I hope that I will be able to record more data with the group during my last month at Stony Brook.

Bibliography

[1] P.W. Milonni, J.H. Eberly, *Lasers* (John Wiley & Sons, New York, NY 1988)

[2] E. Hecht, *Optics*, 4th edn. (Addison–Wesley, San Francisco, Ca 2002)

[3] O. Svelto, *Principles of Lasers*, 3rd edn. (Plenum Press, New York, NY 1989)

[4] A. Siegman, *Lasers* (University Science Books, Mill Valley, Ca 1986)

[5] A. Yariv, *Quantum Electronics*, 2nd edn. (John Wiley & Sons, New York, NY 1975)

[6] B.B. Laud, *Lasers and Nonlinear Optics*, 2nd edn. (Wiley Eastern Ltd., New Delhi, India 1991)

[7] A.C. Newell, J.V. Moloney, *Nonlinear Optics* (Addison–Wesley, Redwood City, Ca 1992)

[8] R.W. Boyd, *Nonlinear Optics* (Academic Press, San Diego, Ca 1992)

[9] G.P. Agrawal, R.W. Boyd (editors), *Contemporary Nonlinear Optics* (Academic Press, San Diego, Ca 1992)

[10] S.A. Akhmanov, V.A. Vysloukh, A.S. Chirkin, *Optics of Femtosecond Laser Pulses* (AIP, New York, NY 1992)

[11] J. Herrmann, B. Wilhelmi, *Lasers for Ultrashort Light Pulses* (North–Holland, Amsterdam, The Netherlands 1987)

[12] W. Kaiser (editor), *Ultrashort Light Pulses* (Springer–Verlag, Berlin, Germany 1988)

[13] D.T. Reid, *Few Cylce EM Pulses*, Contemp. Phys. **40**, 193 (1999)

[14] M. von Ardenne, G. Musiol, S. Reball, *Effekte der Physik*, 2nd edn. (Frankfurt/Main, Germany 1997)

[15] C. Gerthsen, H. Vogel, *Physik*, 17th edn. (Springer–Verlag, Berlin, Germany 1993)

[16] St. Andrews University – W. Sibbett Group Homepage
http://st-andrews.ac.uk/ wsquad/background/modelock/modelock.htm

[17] D.E. Spence, P.N. Kean, W. Sibbett, *60–fsec Pulse Generation from a self–mode–locked Ti:Sapphire Laser*, Opt. Lett. **16**, 42 (1991)

[18] D.E. Spence, J.M. Evans, W.E. Sleat, W. Sibbett, *Regeneratively initiated self–mode–locked Ti:Sapphire Laser*, Opt. Lett. **16**, 1762 (1991)

[19] Kapteyn–Murnane Laboratories L.L.C., *Model TS Ti:Sapphire Laser Kit*, Instruction Manual, (Boulder, Co 2002)

[20] Kapteyn–Murnane Laboratories L.L.C., *High Average Power Ultrafast Amplifier System*, Manual version 1.3, (Boulder, Co 2002)

[21] J. Zhou, G. Taft, C.P. Huang, M.M. Murnane, H.C. Kapteyn, *Pulse Evolution in a broad–bandwidth Ti:Sapphire Laser*, Opt. Lett. **19**, 1149 (1994)

[22] I.D. Jung, F.X. Kärtner, N. Matuschek, D.H. Sutter, F. Morier–Genoud, G. Zhang, U. Keller, V. Scheuer, M. Tilsch, T. Tschudi, *Self–starting 6.5–fs pulses from a Ti:Sapphire Laser*, Opt. Lett. **22**, 1009 (1997)

[23] U. Morgner, F.X. Kärtner, S.H. Cho, Y. Chen, H.A. Haus, J.G. Fujimoto, E.P. Ippen, V. Scheuer, G. Angelow, T. Tschudi, *Sub–two–cycle Pulses from a Kerr–Lens Mode–locked Ti:Sapphire Laser*, Opt. Lett. **24**, 411, (1999)

[24] S. Backus, C.G. Durfee III, M.M. Murnane, H.C. Kapteyn, *High Power Ultrafast Lasers*, Rev. Sci. Instrum. **69**, 1209 (1998)

[25] R. Trebino, D.J. Kane, *Using Phase Retrieval to measure the intensity and phase of ultrashort Pulses: Frequency–Resolved Optical Gating*, J. Opt. Soc. Am. A **10**, 1101 (1993)

[26] D.N. Fittinghoff, J.L. Bowie, J.N. Sweetser, R.T. Jennings, M.A. Krumbügel, K.W. DeLong, R. Trebino, I.A. Walmsley, *Measurement of the Intensity and Phase of ultraweak, ultrashort Laser Pulses*, Opt. Lett. **21**, 884 (1996)

[27] A. Sullivan, W.E. White, K.C. Chu, J.P. Heritage, K.W. DeLong, R. Trebino, *Quantitative Investigation of optical phase–measuring Techniques for ultrashort Pulse Lasers*, J. Opt. Soc. Am. B **13**, 1965 (1996)

[28] R. Trebino, K.W. DeLong, D.N. Fittinghoff, J.N. Sweetser, M.A. Krumbügel, B.A. Richman, *Measuring ultrashort Laser Pulses in the time–frequency Domain using Frequency–Resolved Optical Gating*, Rev. Sci. Instrum. **68**, 3277 (1997)

[29] J.H. Moore, C.C. Davis, M.A. Coplan, *Building Scientific Apparatus*, 2nd edn. (Addison–Wesley, Redwood City, Ca 1989)

[30] T.A. Delchar, *Vacuum Physics and Techniques* (Chapman & Hall, London, United Kingdom 1993)

[31] G. Scoles (editor), *Atomic and Molecular Beam Methods* (Oxford University Press, New York, NY 1988)

[32] Del Mar Ventures, *Microchannel Plates Broschure* (San Diego, Ca 2002)

[33] W.C. Wiley, I.H. McLaren, *Time–of–Flight Mass Spectrometer with improved Resolution*, Rev. Sci. Instrum. **26**, 1150 (1955)

[34] R.J. Cotter (editor), *Time–of–Flight Mass Spectroscopy* (American Chemical Society, Washington, DC 1994)

[35] D.E. Schilke, R.J. Levis, *A Laser Vaporization, Laser Ionization Time–of–Flight Mass Spectrometer for the Probing of fragile Biomolecules*, Rev. Sci. Instrum. **65**, 1903 (1994)

[36] J.D. Pinkston, M. Rabb, J.T. Watson, J. Allison, *New Time–of–Flight Mass Spectrometer for improved Mass Resolution, Versatility, and Mass Spectroscopy/Mass Spectrometry Studies*, Rev. Sci. Instrum. **57**, 583 (1986)

[37] K. Ueda, E. Shigemasa, Y. Sato, A. Yagashita, T. Sasaki, T. Hayaishi, *High Resolution Time–of–Flight Methods for Studies on Ionic Fragmentation of Molecules*, Rev. Sci. Instrum. **60**, 2193 (1989)

[38] B.J. Pearson, J.L. White, T.C. Weinacht, P.H. Bucksbaum, *Coherent Control using adaptive Learning Algorithms*, Phys. Rev. A **63**, 063412 (2001)

[39] D. Zeidler, S.Frey, K.L. Kompa, M. Motzkus, *Evolutionary Algorithms and their Application to optical Control Studies*, Phys. Rev. A **64**, 023420 (2001)

[40] A. Assion, T. Baumert, M. Bergt, T. Brixner, B. Kiefer, V. Seyfried, M. Strehle, G. Gerber, *Control of chemical Reactions by feedback–optimized phase–shaped femtosecond Laser Pulses*, Science **282**, 919 (1998)

[41] T. Brixner, N.H. Damrauer, P. Niklaus, G. Gerber, *Photoselective adaptive femtosecond Quantum Control in the liquid Phase*, Nature **414**, 57 (2001)

[42] National Institute for Standards and Technology Chemistry Webbook http://webbook.nist.gov/chemistry/ion-ser.html

[43] D. Hseuh, *Vacuum Systems*, Brookhaven National Laboratory SNS Control Group Homepage
http://www.sns.bnl.gov/jennytest1/doc/2-8-2001/Seminar%20%202–2001%2%20UHV.pdf

[44] F.L. Légaré, J.M. Fraser, D.M. Villeneuve, P.B. Corkum, *Adaptive compression of intense 250–nm–bandwidth laser pulses*, Appl. Phys. B **74**, S279 (2002)

[45] R.J. Levis, H.A. Rabitz, *Closing the Loop on Bond Selective Chemistry Using Tailored Strong Field Laser Pulses*, J. Phys. Chem. A **106**, 6429 (2002)

[46] M.J. DeWitt, R.J. Levis, *Concerning the Ionization of Large Polyatomic Molecules with intense ultrafast Lasers*, J. Chem. Phys. **110**, 11368 (1999)

[47] R.J. Levis, M.J. DeWitt, *Photoexcitation, Ionization, and Dissociation of Molecules using intense near–infrared Radiation of Femtosecond Duration*, J. Phys. Chem. A **103** (1999)

[48] S.K. Shin, H.L. Kim, C.R. Park, *Two Photon Dissociation of Benzene, Phenylacetylene, and Benzaldehyde at 243 nm: Translational Energy Releases in the H Atom Channel*, Bull. Korean Chem. Soc. **23**, 286 (2002)

[49] W. Radloff, T. Freudenberg, H.H. Ritze, V. Stert, F. Noack, I.V. Hertel, *Lifetime of the Benzene Dimer in the* S_2 *electronic State*, Chem. Phys. Lett. **261**, 301 (1996)

[50] L.Lehr, R. Weinkauf, E.W. Schlag, *Separation of neutral versus cationic Dissociation Processes in an ultracompact double Time–of–Flight Spectrometer: first Results on* CH_3I, Int. J. Mass Spectrom. Ion Processes **206**, 191 (2001)

[51] C. Wu, H. Re, T. Liu, R. Ma, H. Yang, H. Jiang, Q. Gong, *Laser–induced Dissociation and Explosion of Methane and Methanol*, J. Phys. B: At. Mol. Opt. Phys. **35**, 2575 (2002)

[52] X.P. Tang, S.F. Wang, M.E. Elshakre, L.R. Gao, Y.L. Wang, H.F. Wang, F.A. Kong, *The field–assisted stepwise Dissociation of Acetone in an intense Femtosecond Laser Field*, J. Phys. Chem. **107**, 13 (2003)

[53] S. Couris, E. Koudoumas, S. Leach, C. Fotakis, *Polarization Effects on the Ionization of Molecules under picosecond and femtosecond Laser Excitation*, J. Phys. B: At. Mol. Opt. Phys. **32**, L439 (1999)

[54] A.M. Müller, C.J.G.J. Uiterwaal, B. Witzel, J. Wanner, K.L. Kompa, *Photoionization and Photofragmentation of gaseous Toluene using 80–fs, 800–nm laser pulses*, J. Chem. Phys. **112**, 9289 (2000)

[55] S.M. Mahurin, R. Sullivan, R.N. Compton in: J.E. Parks, J.P. Young (editors), *Resonance Ionization Spectroscopy 2000* (AIP, Melville, NY 2001)

[56] M.P. Hertlein, *Resonance Effects in Above–Threshold Ionization*, PhD thesis, University of Michigan at Ann Arbor (2000)

[57] S.W. North, D.A. Blank, J.D. Gezelter, C.A. Longfellow, Y.T. Lee, *Evidence for stepwise Dissociation Dynamics in Acetone at 248 and 193 nm*, J. Chem. Phys. **102**, 4447 (1994)

[58] J.C. Owrutsky, A.P. Baronavski, *Ultrafast Photodissociation Dynamics of the S_1 and S_2 States of Acetone*, J. Chem. Phys. **110**, 11206 (1999)

[59] F.H.M. Faisal, *Theory of Multiphoton Processes* (Plenum Press, New York, NY 1987)